Aging and Disease
www.aginganddisease.org
Early access date: July 26, 2025
http://dx.doi.org/10.14336/AD.2025.0484

Original Article

Amyloid Beta Regulates Astrocytic Glucose Metabolism and Insulin Signaling in Experimental Models of Alzheimer's Disease

Melisa Bentivegna[1,2], Carlos Pomilio[1,2], Melina Bellotto[1,2], Nicolás González Pérez[1,2], Soledad P Rossi[3,4], Amal Gregosa[1,2], Daiana Vota[2], Fátima Merech[2], María Marta Bonaventura[5,6], Jessica Presa[1,2], Ángeles Vinuesa[1,2], Victoria Lux-Lantos[5], Soledad Porte Alcón[2], Flavia Saravia[1,2], Juan Beauquis[1,2*]

[1]Laboratory of Neurobiology of Aging, Institute of Biology and Experimental Medicine (IBYME), National Research Council (CONICET) and IBYME Foundation, Buenos Aires, Argentina. [2]Department of Biological Chemistry, Faculty of Exact and Natural Sciences, University of Buenos Aires, Buenos Aires, Argentina. [3]Laboratory of Testicular Neuro-Immuno-Endocrinology, Institute of Biology and Experimental Medicine (IBYME), National Research Council (CONICET) and IBYME Foundation, Buenos Aires, Argentina. [4]Department of Human Biochemistry, Faculty of Medicine, University of Buenos Aires, Buenos Aires, Argentina. [5]Laboratory of Neuroendocrinology, Institute of Biology and Experimental Medicine (IBYME), National Research Council (CONICET) and IBYME Foundation, Buenos Aires, Argentina. [6]School of Science and Technology, National University of San Martín (UNSAM), Buenos Aires, Argentina.

[Received April 9, 2025; Revised July 19, 2025; Accepted July 21, 2025]

ABSTRACT: Alzheimer's disease (AD) is the most prevalent neurodegenerative disorder, characterized by amyloid beta (Aβ) plaques, neuroinflammation and cognitive impairment. Metabolic disturbances, particularly brain insulin resistance, are increasingly recognized as central features of AD pathophysiology. Astrocytes, essential for brain energy metabolism, exhibit a loss of homeostatic functions in AD, possibly promoting neurodegeneration. Even though the main astrocytic glucose transporters are non-insulin dependent, insulin may regulate astroglial glucose metabolism. Our objective was to evaluate insulin signaling and astrocyte metabolism in the PDAPP-J20 transgenic mouse model of familial AD and in mouse primary astrocyte cultures exposed to Aβ. Adult PDAPP-J20 mice showed hyperinsulinemia, hippocampal insulin resistance and astrocytic proinflammatory activation. The reactive glial phenotype was accompanied by decreased insulin receptor levels in this chronic setting. Exposure of primary astrocytes to Aβ induced proinflammatory activation, oxidative stress and loss of glutamate transporter EAAT2, crucial for neuroprotection. Even though Aβ-exposed astrocytes showed increased insulin receptor levels in this acute setting, insulin-induced phosphorylation of the receptor was hampered. Amyloid-treated astrocytes also showed increased glucose uptake, lactate release and glycogen storage. Insulin treatment was associated with a recovery of mitochondrial membrane potential and increased amyloid uptake, highlighting a pro-homeostatic role for the hormone. Our results highlight the interplay between insulin signaling and astrocyte metabolism at different experimental and temporal settings of amyloid pathology. Understanding these mechanisms may help to design therapeutic strategies aimed at restoring metabolic balance and mitigating neurodegeneration.

Key words: Alzheimer's disease, amyloid, astrocytes, insulin resistance, glucose, metabolism

***Correspondence should be addressed to:** Dr. Juan Beauquis. Laboratory of Neurobiology of Aging, Institute of Biology and Experimental Medicine (IBYME-CONICET). Correspondence: Vuelta de Obligado 2490, Lab. 1210, zip code: 1428, Buenos Aires, Argentina. Email: j.beauquis@ibyme.org.ar

INTRODUCTION

Alzheimer's disease (AD) is the main cause of dementia and a highly prevalent pathology in elderly groups [1]. Its main hallmarks are amyloid beta (Aβ) plaques and neurofibrillary tangles which trigger brain inflammation, neurodegeneration and cognitive impairment. Many of its pathological characteristics are shared with the physiological aging process, showing deficits in multiple basic cellular processes and neurological functions. Among the main impaired functions in AD and aging is brain metabolic homeostasis [2–4]. In this sense, brain insulin resistance has been proposed as a link between aging, diabetes and AD, considering that these conditions show variable degrees of insulin resistance, increased reliance on glycolysis for meeting neuronal energy needs and elevated extracellular lactate, among other changes [5, 6].

Brain insulin resistance [7], mitochondrial dysfunction [8] and bioenergetic alterations [9] are usual findings in AD patients and in experimental models. Interestingly, one of the brain regions early affected in the context of AD is the hippocampus, a structure that displays a high concentration of insulin receptors and participates, along with the hypothalamus, in the regulation of central and peripheral glucose levels [10, 11]. However, there is no consensus regarding the dynamics and characteristics of the brain metabolic changes that occur in AD. While hypometabolism has predominated in the descriptions of AD progression, in recent years more attention has been directed to the pathophysiological role of brain hypermetabolism [12, 13].

In this context, astrocytes play a key role, showing an enrichment in these metabolic pathways compared with other neural cells [14]. Astrocytes are vital for the provision of energy substrates for neurons, participating in glucose uptake from blood vessels, glycolysis, glycogen buildup and lactate secretion [15]. While neurons have the highest energy requirements in the brain and are able to uptake glucose, astrocytes uptake glucose at a much higher rate, supporting the hypothesis of the 'lactate shuttle' for maintaining brain energy homeostasis [16]. In AD, astrocytes adopt diverse but usually concurrent phenotypes, showing proinflammatory reactivity and homeostatic dysfunction [17]. Given their key role in brain energy metabolism and neuroprotection, the loss of astrocytic homeostatic functions could be a central event in the course of AD [18].

In AD, there are deficits in astrocytic glycolysis, an event that could interfere with lactate shuttling [2]. Also, key astroglial metabolites such as pyruvate, 2-oxoglutarate and glutamine, as well as pathways such as glycolysis, the TCA cycle and glutamate metabolism, were found to be disturbed in the transcriptional analysis of brains from AD patients [19]. Classically, the brain was considered an insulin-insensitive tissue as most glucose transporters in the brain are not directly regulated by insulin. Now, there is evidence that insulin has multiple roles in the brain as a neurotrophic factor, affecting memory and behavior, modulating neurovascular coupling and as a metabolic regulator, both centrally and peripherally [20]. However, there is scarce information regarding the role of insulin in the regulation of astrocyte metabolic functions that could be relevant for AD pathophysiology. Recent studies have highlighted that impaired insulin signaling in the brain disrupts astrocyte metabolic functions, including glucose uptake and mitochondrial activity, thereby exacerbating neuro-degenerative processes in AD models [21]. Moreover, insulin resistance in astrocytes impairs their ability to support neuronal metabolism and synaptic function, contributing to cognitive decline [22].

This background led us to analyze the metabolic changes that occur in *in vivo* and *in vitro* models of AD-like amyloid pathology, focusing on insulin signaling and regulation of astrocyte responses. In the PDAPP-J20 transgenic mouse model of familial AD, we found a metabolic disturbance associated with cognitive impairment and hippocampal insulin resistance along with astrocyte proinflammatory reactivity. Additionally, we found subtle sex-dependent alterations in hippocampal insulin signaling. Upon *in vitro* Aβ exposure, primary astrocytes showed proinflammatory activation and a complex metabolic phenotype related to cell energetics and insulin signaling. Understanding the metabolic response of astrocytes in the context of AD pathogenesis could help design therapeutic interventions centered in rescuing brain homeostasis.

MATERIALS AND METHODS

Animals

Adult male and female PDAPP-J20 transgenic mice (Tg; full designation Tg(PDGFB-APPSwInd)20Lms) along with their non-transgenic (NTg) littermates were bred at the Institute of Biology and Experimental Medicine Animal Facility (IBYME-CONICET; NIH Assurance Certificate # A5072-01). These mice were maintained on a C57BL/6J genetic background through heterozygous crosses, with housing conditions controlled for temperature (22°C), humidity (50%), and light cycles (12 h/12 h). Mice were fed *ad libitum* with standard mouse chow from GEPSA Feeds, Argentina (http://gepsafeeds.com/animales-de-bioterio/). Diet composition: Proteins: 25.5%; Carbohydrates: 28.8%; Fat: 3.6%; Fiber: 5.5%; Calcium (min-max): 1.15-1.25%; Phosphorus (min-max):

0.85-0.95%; Total minerals: 10%; Energy value: 2,500 Kcal/kg (metabolizable energy). The breeding stock for these mice was generously provided by Dr. Verónica Galván from the University of Oklahoma Health Sciences Center. These transgenic mice carry the human amyloid precursor protein (APP) gene with Swedish (KM670/671NL) and Indiana (V717F) mutations, which are associated with familial AD [23]. Transgenic mice were genotyped through PCR with specific human APP primers. Non-transgenic mice were used as controls. All experimental procedures adhered to the NIH Guidelines for the Care and Use of Laboratory Animals and received approval from the IACUC of the Institute of Biology and Experimental Medicine (protocol #23/2023). Blood glucose data were collected under isoflurane-free conditions to avoid anesthesia-induced hyperglycemia confounding results. To optimize animal welfare, cohort sizes were minimized through power calculations (see statistics section). Every effort was made to minimize animal suffering and discomfort. Weight and 6 h-fasting glycemia were measured using a glucometer (One Touch Ultra, Johnson & Johnson, Argentina). Euthanasia at 8 months followed a two-phase protocol. An intraperitoneal injection of ketamine (80 mg/kg; Holliday-Scott) and xylazine (10 mg/kg; Bayer) was used to achieve surgical-plane anesthesia, ensuring absence of paw withdrawal reflex. Then, decapitation during deep anesthesia was performed for immediate trunk blood collection, minimizing postmortem metabolic changes in insulin measurements (radioimmunoassay).

Behavioral testing

Open-field test. An open-field exploration test was performed to evaluate exploratory behavior. The apparatus consisted of a wooden platform measuring 55 × 55 cm, coated with white melamine, and enclosed by 25-cm-high walls. Each animal was placed individually in the center of the arena, and exploratory behavior was recorded for 5 minutes using video recordings. A central region, digitally defined as a 15 × 15 cm area, was established for analysis. The total distance traveled and the distance traversed within the central region were assessed using EthoWatcher software [24] and AnyMaze (Stoelting Co.).

Barnes Maze. The Barnes Maze was used to assess the learning ability and long-term spatial memory. The maze consisted of a brightly lit, circular platform (85 cm in diameter) with 20 equidistant holes located in the periphery of the arena, one of which served as the target escape leading to a dark box. The walls of the behavior room featured large spatial clues: a red door, a black table, a metallic sink and a large blue box. Mice underwent four trials per day over four consecutive days (acquisition phase), with each trial ending when the animal entered the dark box. On day five, 24 h after the last training session, a probe trial was conducted without the escape box and the latency to the target hole was recorded.

Tissue processing and immunohistochemistry

Following euthanasia, one brain hemisphere was dissected and fixed overnight in 4% paraformaldehyde. Subsequently, it was coronally sectioned into 60 µm slices using a vibrating microtome (PELCO easiSlicer, Ted Pella, USA). Sections containing the hippocampus were stored in a cryoprotectant solution (PBS:ethylene glycol:glycerine, 2:1:1) at -20°C until further processing. For immunohistochemical and immunofluorescence analyses, six serial brain sections per mouse were selected. A free-floating technique was employed to detect glial fibrillary acidic protein (GFAP) and S100B using rabbit polyclonal antibodies (GFAP, 1:300, G-9269 or S100B, 1:500, ABN59) and a mouse monoclonal antibody (GFAP, 1:300, G-3893, Sigma, USA). First, sections were thoroughly rinsed with PBS to eliminate the cryoprotectant solution. Then, nonspecific antigenic sites were blocked with goat normal serum. Sections were incubated overnight with the primary antibodies. Subsequently, sections were incubated with corresponding secondary fluorescent antibodies (Alexa 488/555 anti-rabbit and anti-mouse, 1:1000, Invitrogen, USA). Specificity of the immunostaining was determined in controls processed without the primary antibody (secondary antibody-only controls). For the representative images in the figures, we selected those that better showed the immunostaining pattern of interest and that displayed a similar zone of the hippocampus in both groups.

S100B and GFAP immunoreactive area.

The S100B label was quantified for each GFAP+ astrocyte. For this, 5-6 astrocytes per hilus were randomly selected using the nuclear label with DAPI as a reference. After selecting each astrocyte, thresholds were established for GFAP and S100B and the % area of each GFAP-positive astrocyte occupied by S100B was determined for each cell. Six brain sections per animal were evaluated, obtaining an average of 30 cells.

IR puncta quantification and GFAP immunoreactive area

Confocal images of coronal hippocampal sections (*stratum radiatum*) immunolabeled with anti-GFAP and IR antibodies were acquired at 60X magnification. Image processing was performed in FIJI using the Olympus Viewer plugin. Individual cells were manually selected,

and a square region of interest (ROI) was defined for each. Background was subtracted using the "Rolling Ball" function, and images from each channel were averaged to generate Z-stacks.

The GFAP+ immunoreactive area of astrocytes was determined by applying a threshold to each ROI. Additionally, merging the GFAP and IR Z-stacks allowed quantification of IR+ puncta colocalizing with GFAP. For each animal, at least four serial coronal sections were analyzed, with 2–3 confocal images per section and a minimum of 20 GFAP+ cells evaluated (3 animals per group). Results were expressed as the average cell immunoreactive area per image for GFAP and as the average number of IR+ puncta in a cell per image within the GFAP-positive area.

Cell culture

Primary cell cultures were obtained from postnatal day 1–2 C57BL/6 mice. After decapitation, brains were extracted, and the meninges, brainstem, and cerebellum were removed under a stereomicroscope. The cerebral hemispheres, immersed in DMEM/F12 (D0547, Sigma-Aldrich), were dissected with a scalpel and further homogenized using a serological pipette. Following a brief ice incubation, the supernatant was collected, centrifuged, and the resulting pellet—comprising cells from two hemispheres—was resuspended in 1 mL of medium and seeded into T75 flasks pretreated with poly-L-lysine (P4707, Sigma). Cultures maintained in DMEM/F12 supplemented with 10% fetal bovine serum (FBS; #FRA, Internegocios, Argentina) reached confluency after 7–10 days. Microglia were eliminated by vigorous shaking for 48 hours and subsequent 24-hour incubation with 5-fluorouracil (F6627, Sigma) to prevent their proliferation. Finally, after an additional 24 hours in DMEM/F12 with 10% FBS and penicillin-streptomycin (P0781, Sigma), astrocytes were detached with 0.125% trypsin (T4799, Sigma) for plating.

Amyloid preparation/exposure protocol

Primary astrocytes were exposed to fibrillar amyloid $\beta_{1\text{-}42}$ (#20574, Cayman Chemicals) as an *in vitro* model of AD. To generate the fibrillar state, beta amyloid was partially diluted in distilled water and incubated under sterile conditions at 37 °C for 72 hours, a commonly used method to promote fibrillization while minimizing confounding factors related to solvents or buffer components [25, 26]. Once the fibrillar solution was obtained, the appropriate dilutions (0.5 μM or 0.05 μM) were prepared in DMEM/F12 according to the treatment requirements.

Insulin treatment

To stimulate cells with insulin, a stock solution diluted in sterile saline was prepared and adjusted to the required concentrations in DMEM/F12 or glucose-free RPMI, depending on the experiment. For insulin signaling assays, cells were treated with 1 μM insulin in DMEM/F12 supplemented with 10% FBS for 2 h. For glucose uptake and lactate release assays, insulin was added to the wells to achieve a final concentration of 1 μM for 1 hour. Finally, in the MitoTracker Red assay, cells were co-incubated with 1 μM insulin and 0.5 μM $A\beta_{1\text{-}42}$ for 24 h.

Immunocytochemistry

Cells attached to coverslips were fixated with methanol, permeabilized with 0.5% triton X-100 in PBS and unspecific binding sites were blocked with 1% BSA in PBS. Cells were incubated with primary antibodies for GFAP, S100B, NFκB (rabbit polyclonal, 1:1000, sc-372, SCBT, USA), GLT1/EAAT2, GLUT1 (rabbit polyclonal, 1:500, ab652, Abcam), IR (rabbit polyclonal, 1:500, ab137747, Abcam) and Aβ (4G8 mouse monoclonal, 1:1000, MAB1561, Chemicon, USA), and then with Alexa Fluor- (488/596; Invitrogen, Thermo Fisher, USA) labeled secondary antibodies. Nuclei were visualized with DAPI (D9542, Sigma, USA) and coverslips were mounted on glass slides with PVA-DABCO (Sigma, USA). For NFκB immunostaining, a positive control for nuclear translocation was performed by incubating with lipopolysaccharide (LPS; Sigma) at 100 ng/mL. For the representative images in the figures, we selected those that showed comparable fields between groups regarding cell size, number and density.

2-NBDG and fluorometer/Incucyte Imaging

Fluorometer. Primary astrocytes were seeded at 15,000 cells per well in 96-well plates and cultured to confluency (approximately 3 days). Cells were then stimulated with 0.5 μM fibrillar $A\beta_{1\text{–}42}$ in DMEM/F12 supplemented with 10% FBS for 1 hour. The medium was subsequently replaced with glucose-free RPMI (Sigma) containing 0.5 μM Aβ1–42, 1 μM insulin, and 100 μM 2-NBDG (N13195; Invitrogen), and the cells were incubated at 37 °C in the dark for 1 hour. After incubation, the medium was removed, wells were briefly washed with PBS, and 100 μL of DMSO was added per well. Cells were lysed by performing three cycles of pipetting, and the lysate was transferred to a black 96-well plate. Fluorescence was measured in each well using an Advanced multimode microplate reader (Spark).

Incucyte Imaging. A total of 35,000 cells per well were seeded in 24-well plates and allowed to reach confluence over approximately three days. The cells were then treated with 0.5 µM fibrillar $A\beta_{1-42}$ in DMEM/F12 supplemented with 10% FBS for 24 hours. In addition to fibrillar $A\beta_{1-42}$, a group of cells were treated with BMS-536924 (14666, Cayman Chem.) at a concentration of 1 µM or NVP-ADW742 (18390, Cayman Chem.) at 5 µM. Both compounds were incubated simultaneously for 24 hours in the presence of $A\beta_{1-42}$ 0.5 µM, using DMEM/F12 medium supplemented with 10% FBS. Following stimulation, the medium was removed and replaced with glucose-free RPMI (R1383, Sigma), to which 1 µM insulin, and 100 µM 2-NBDG were added. The samples were then incubated at 37°C in darkness for 1 hour. Subsequently, the medium was removed, and Earle's buffer was added. Immediately after, the plates were placed in the Incucyte Live-Cell Analysis System (Sartorius), an automated imaging and analysis platform designed to continuously monitor and quantify cellular dynamics in real time. The Incucyte system captured high-resolution fluorescence images.

Lactate measurement

Primary astrocytes were seeded at 15,000 cells per well in 96-well plates and cultured to confluency (approximately 3 days). After treatment, two protocols were used for medium collection: one protocol involved washing the cells and incubating with serum-free DMEM/F12 for 2 hours, while the other involved incubating with Earle's buffer for 1 hour. In both cases, conditioned media were collected. Lactate release was quantified using the Roche colorimetric lactate assay (11822837, Roche, Germany), which relies on the enzymatic oxidation of lactate to pyruvate by lactate oxidase, generating H_2O_2 as a byproduct. Initially, 90 µL of reagent 1 was added to each well followed by 10 µL of sample, and after a 5-minute incubation at 37 °C, absorbance was measured at 492 nm. Subsequently, 18 µL of reagent 2 was added, and following a 15-minute incubation at 37 °C, the final absorbance at 492 nm was recorded to determine lactate concentration.

Glycogen measurement

After treatments, cells were fixed with cold methanol for 5 minutes, washed twice with 70% ethanol, and incubated with periodic acid (Biopack, Argentina) for 30 minutes to oxidize secondary alcohol groups in glucose rings and generate free aldehydes. Following three additional washes with 70% ethanol, cells were incubated for 1 hour with Schiff reagent (basic fuchsin decolorized with sulfur dioxide; Biopack, Argentina), which reacts with the aldehydes to produce a characteristic purple-pink coloration. Finally, cells were washed with PBS, stained with DAPI, and coverslips were mounted using PVA-DABCO mounting medium.

MitoSOX, MitoTracker, BODIPY and MitoSpy probes staining

MitoSOX Red (M36007, Invitrogen), a cationic derivative of dihydroethidium (DHE), was used to detect mitochondrial-derived superoxide anion. In the presence of this radical, DHE is oxidized to form 2-hydroxymitoethidium (excitation: 510 nm; emission: 580 nm). Cells were incubated with 5 µM MitoSOX Red in PBS for 15 minutes at 37 °C, fixed with 4% PFA for 15 minutes, washed with PBS, stained with DAPI, and coverslips were mounted with PVA-DABCO.

MitoTracker Red CMXROS (M7512, Invitrogen) was used to stain mitochondria based on their membrane potential, allowing evaluation of mitochondrial morphology and functionality. BODIPY 493/503 (D3922, Invitrogen) was employed to stain neutral lipids for identification and quantification of cytoplasmic lipid droplets. MitoTracker Red was used in a concentration of 500 nM and BODIPY 493/503 10 µM in DMEM/F12 without serum. Cells were incubated with these solutions for 30 minutes at 37 °C, fixed with 4% PFA, washed with PBS, stained with DAPI, and coverslips were mounted with PVA-DABCO.

MitoSpy Green (424805, Biolegend) was used for specific mitochondrial staining, providing accurate visualization of total mitochondrial content independent of membrane potential. Cells were incubated with 250 nM MitoSpy Green in DMEM/F12 without serum for 30 minutes at 37 °C and then fixed with 4% PFA.

Etomoxir treatment

To evaluate the effect of etomoxir (a β-oxidation inhibitor; E1905, Sigma-Aldrich) on lipid droplets and mitochondrial membrane potential in primary astrocyte cultures, cells were treated with etomoxir at a concentration of 10 µM. The treatment was applied 30 minutes before exposure to $A\beta_{1-42}$ at 0.5 µM and maintained simultaneously for 2 or 24 hours. At the end of the stimulation protocol, cells were incubated with MitoTracker Red to label mitochondria and BODIPY 493/503 Green to detect lipid droplets, as described in the corresponding section.

Quantification of immunofluorescence images

Individual cell areas from spatially calibrated images were outlined and measured before applying a threshold to

measure immunopositive areas for each fluorophore. The analysis of co-localization between S100B and GFAP markers was done using the JACoP plug-in [27] and expressed as the percentage or GFAP+ areas that were also positive for S100B. Nuclear translocation of NFκB was evaluated by a qualitative score done on at least 30 cells per culture well. We assigned a 0 value for cells with evident higher fluorescence in the cytoplasm than in the nucleus, a 1 value for cells with equal cytoplasmic/ nucleus staining and 2 for cells with evident higher nucleus than cytoplasmic staining. The resulting score was averaged for all cells in each sample. Higher values indicated higher nuclear translocation. Quantification of Aβ immunofluorescence was done using ImageJ software.

Immunoblot

Primary astrocyte cultures were seeded in 6-well plates at approximately 250,000 cells per well and grown to confluence (5–7 days) prior to experimental treatments. Cells were incubated with $A\beta_{1-42}$ (0.5 μM) in DMEM/F12 supplemented with 10% FBS for 2 or 24 hours. In separate experiments, 1 μM insulin was applied either for 2 hours following Aβ removal or during the final 2 hours of Aβ incubation. After treatment, cells were rapidly washed with PBS and harvested using a lysis buffer and a scraper. Protein concentrations were determined using the Bradford assay, and samples were normalized and stored at −20 °C until further use. For Western blot analysis, 30 μg of protein per lane was resolved by SDS-PAGE and transferred to membranes, which were probed with antibodies against phosphorylated IR (pIR Y1361, 1:500; ab60946, Abcam), phosphorylated Akt (pAkt S473, 1:500; #9271, Cell Signaling), total IR (1:500, ab137747, Abcam), total Akt (1:500; #9272, Cell Signaling), and actin (1:200, sc-47778, Santa Cruz).

Statistical analysis

The acquisition and analysis of experimental data were performed under blind conditions regarding group information. Statistical analyses involved unpaired one- or two-tailed Student's t-test, one-way or two-way ANOVA with Sidak's, Tukey's or Dunnett's *post hoc* tests as detailed for each experiment in the Results section and were performed with Prism 9.0 (GraphPad Software Inc.). Normality of the data was checked using the Shapiro-Wilk test. In experiments where the n was too small to determine normality, non-parametric tests were used as detailed in each figure legend (Mann Whitney or Kruskal Wallis tests). Data are expressed as mean ± SEM. The sample size was determined using StatMate 2.0 (GraphPad Software Inc.), drawing on data from previous studies. The calculation aimed to achieve a statistical significance of 5% ($\alpha = 0.05$) with a statistical power of 80% to detect differences of at least 10% between groups. This approach ensured that the study had sufficient power to identify meaningful effects while minimizing the number of animals used. The reported p values were adjusted for multiple comparisons (in Sidak's, Tukey's and Dunnett's tests). The number and type of replicates for each experiment is detailed in the corresponding figure legends.

RESULTS

PDAPP-J20 transgenic mice showed high insulinemia, anxiety-like behavior and cognitive impairment

Firstly, metabolic and behavioral parameters were analyzed in male and female 8-month-old PDAPP-J20 transgenic mice, a familial AD model (Fig.1A). At 8 months of age this model exhibits cognitive impairment, hippocampal extracellular amyloid plaques and increased glial reactivity [28]. While the current study focuses on astrocyte-specific mechanisms, we and others have previously characterized neuronal populations and synaptic alterations in this transgenic model [28–30]. In order to characterize a general metabolic profile of control and PDAPP-J20 transgenic mice, we analyzed fasting glycemia and insulinemia. Transgenic (Tg) and control (NTg) mice showed similar glycemia (Fig.1B-C), regardless of the sex analyzed. The analysis of insulinemia by radioimmunoassay showed a genotype effect with higher levels in Tg mice (Two-way ANOVA, genotype effect $p<0.05$, sex effect $p=0.339$, no differences between groups with the Sidak's *post hoc* test; Fig.1D). Considering this result, we evaluated the pancreatic expression of inflammatory markers to detect potential damage due to insulin overproduction. The expression of interleukin-1β (IL-1β) and cyclooxygenase-2 (COX-2) was similar between Tg and control mice (Supplementary Fig.1A-B). Also, NTg and Tg mice showed similar body weight at the end of the protocol (Supplementary Fig. 2).

To evaluate the behavioral phenotype, mice were tested in an open-field for 5 minutes to measure locomotor activity and anxious-like behavior. Transgenic mice showed similar locomotor activity to control mice in the open-field arena (Supplementary Fig. 3), independently of the sex analyzed. However, both male and female Tg mice exhibited a lower percentage of the distance traveled and time spent in the center of the arena than their respective controls (NTg vs. Tg, males $p<0.005$, females $p<0.01$, Student's t test; Fig.1E-G and Supplementary Fig. 4), an indicator of anxious-like behavior. Learning and memory were evaluated in a Barnes maze using a 4-day, 4-trial/day training scheme followed by a probe test trial 24 h later.

No differences were found in the learning curve between NTg and Tg mice, confirming that all animals were able to learn the location of the target hole and thus validating the subsequent memory test (Two-way RM ANOVA males p=0.6451, females p=0.1099 for genotype effect; Fig.1H-I). However, latencies to the target hole were higher in Tg than in NTg mice on the probe trial, indicating a spatial memory deficit in both sexes (NTg vs. Tg, males p<0.01, females p<0.05, Student's t test; Fig.1J-L).

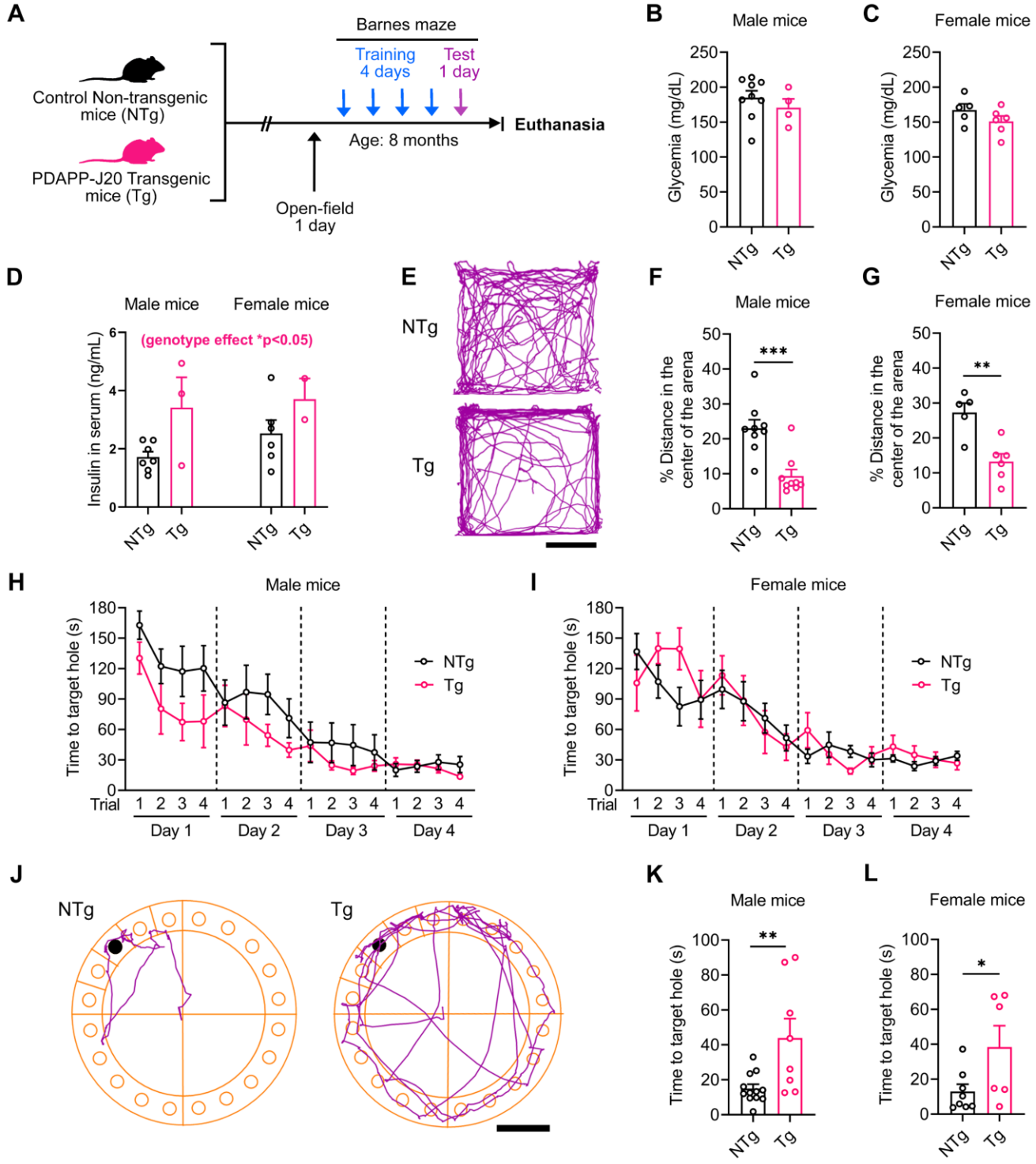

Figure 1. Transgenic mice showed hyperinsulinemia and cognitive deficits. **(A)** Experimental protocol. Metabolic and behavioral parameters were evaluated in 8-month-old male and female PDAPP-J20 transgenic (Tg) and control (NTg) mice. **(B-C)** Glycemia in male and female mice (mg/dL; n for males NTg=9, Tg=4; n for females NTg=5, Tg=6). **(D)** Insulinemia in male and female mice after

a 6-hour fasting (Two-way ANOVA, genotype effect *p<0.05; ng/mL; n for males NTg=7; Tg=3; n for females NTg=4; Tg=2). **(E)** Representative track plots from NTg and Tg mice in the open-field test (5 min). **(F-G)** Percent distance traveled in the center of the open-field arena for male and female mice (Student's *t* test; ***p<0.005, **p<0.01; % distance; n for males NTg=9, Tg=9; n for females NTg=5, Tg=6). **(H-I)** Latency to the target hole in the Barnes maze training trials by day (*D*) and trial (*T*) for male and female mice (180 s tracking; n for males NTg=12, Tg=8; n for females NTg=8, Tg=6). **(J)** Representative track plots in the Barnes maze in the probe trial (day 5; 90 s tracking; n=6-8). **(K-L)** Latency to the target hole in the probe trial of the Barnes maze test for male and female mice (Student's *t* test; **p<0.01, *p<0.05; n for males NTg=12; Tg=8; n for females NTg=8; Tg=6). Scale bars in E and J correspond to 20 cm. The n corresponds to mice per group. All the data are expressed as the means ± SEMs.

Hippocampal insulin signaling was impaired in PDAPP-J20 mice in a sex-dependent manner, coinciding with higher astroglial reactivity and decreased astroglial insulin receptor density

Even though insulinemia was increased in Tg mice (Fig. 1D-E), hepatic activation of Akt after an acute insulin stimulus (5 IU i.p.; 10 min before euthanasia) was not affected by the genotype (Supplementary Fig. 5), suggesting integrity of the pathway at a peripheral level. Phosphorylation of Akt is a downstream event to insulin receptor (IR) activation and constitutes a mechanism through which insulin can exert its neuroprotective effects [31]. However, Akt phosphorylation in the hippocampus of male mice was lower in Tg than in matching controls (NTg vs. Tg, p<0.05, Student's t test; Fig. 2A; complete blots for Figure 2 are presented in Supplementary Fig. 6), suggesting a dampened central response to insulin that could drive hyperinsulinemia. Female Tg mice showed a similar hippocampal pAkt/Akt ratio to their corresponding controls (Supplementary Fig. 7A), indicating a sex-specific disturbance.

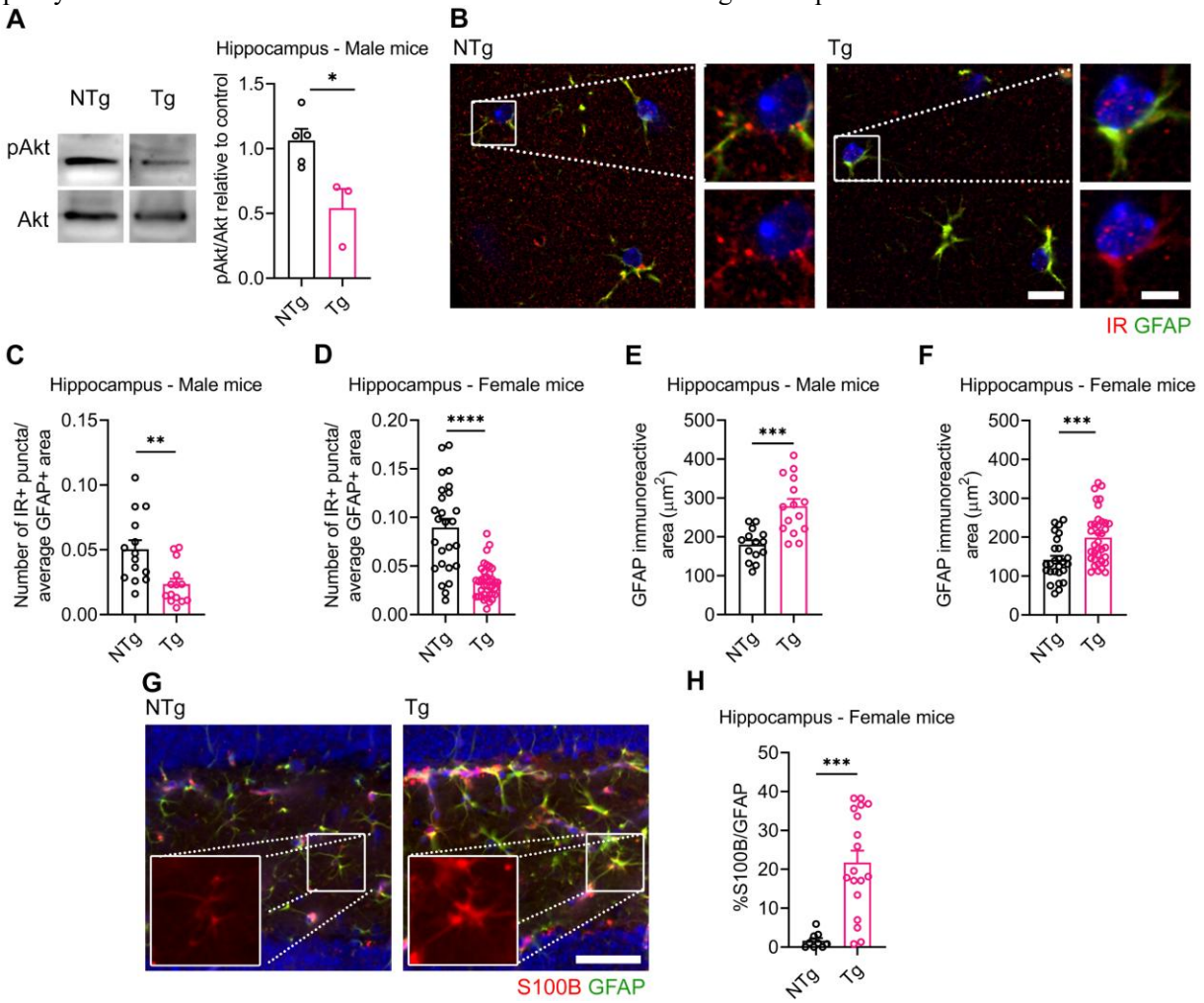

Figure 2. Transgenic mice showed impaired hippocampal insulin signaling and reactive astrocytes with decreased levels of insulin receptor. (A) Immunoblots for pAkt/Akt in protein extracts from hippocampi of male control (NTg) and transgenic (Tg) PDAPP-J20 mice (Mann Whitney test; *p<0.05; n for NTg=5, Tg=3. The ratio shown is relativized to the CTL group. **(B)** Immunofluorescence for IR (red) and GFAP (green) in hippocampal sections of NTg and Tg mice (DAPI counterstain in blue).

Scale bars=20 and 5 µm for large and inset panels, respectively. **(C-D)** Quantification of the number of IR+ puncta/GFAP+ area in male (C) and female (D) mice (Student's *t* test; **p<0.01, ****p<0.001; n for males=14; n for females NTg=27, Tg=37; the n corresponds to confocal fields/group from 3 mice per group). **(E-F)** Quantification of the GFAP+ area in the *stratum radiatum* of male (G) and female (H) NTg and Tg mice (***p<0,005; n for males NTg=14, Tg=15; n for females NTg=26, Tg=36; the n corresponds to confocal fields/group from 3 mice per group). **(G)** Immunofluorescence for S100B (red) and GFAP (green) in the hippocampus (DAPI counterstain in blue). Scale bar=50 µm. **(H)** Quantification of the percentage of S100B+ GFAP+ cells to total GFAP+ cells (**p<0.01, n for NTg=9, Tg=18 confocal fields/group from 3 mice per group). All the data are expressed as the means ± SEMs.

To further understand this result, we sought to analyze levels of IR in the hippocampus, as sustained hyperinsulinemia can downregulate brain IR [32]. Using immunoblotting for IR on female mice hippocampal protein extracts, we found a tendency towards decreased levels in Tg compared with controls (NTg vs. Tg, p=0.0560, Student's t test; Supplementary Fig. 7B), partially supporting our precedent hypothesis. To analyze whether astrocytes contributed to the IR reduction in the hippocampus, we quantified IR+ puncta in GFAP+ astrocytes by immunofluorescence on brain sections (Fig. 2B). Hippocampal astrocytes in both male and female Tg mice showed lower densities of IR puncta than astrocytes in control mice (NTg vs. Tg, males p<0.01, females p<0.001, Student's t test; Fig. 2C-D). Concomitantly, astrocytes from Tg mice showed increased GFAP+ area (NTg vs. Tg, p<0.005 for both sexes, Student's t test; Fig. 2E-F) and higher levels of the S100B marker than controls (NTg vs. Tg, females p<0.01, Student's t test; Fig. 2G-H), suggesting a pro-inflammatory activation accompanying the changes in IR levels. The increased S100B/GFAP ratio has been linked to reactive astrocyte phenotypes and inflammation in AD models [33]. These results support the idea of a metabolic change in the hippocampus of AD mice with concurrent loss of insulin sensitivity and increased astroglial reactivity.

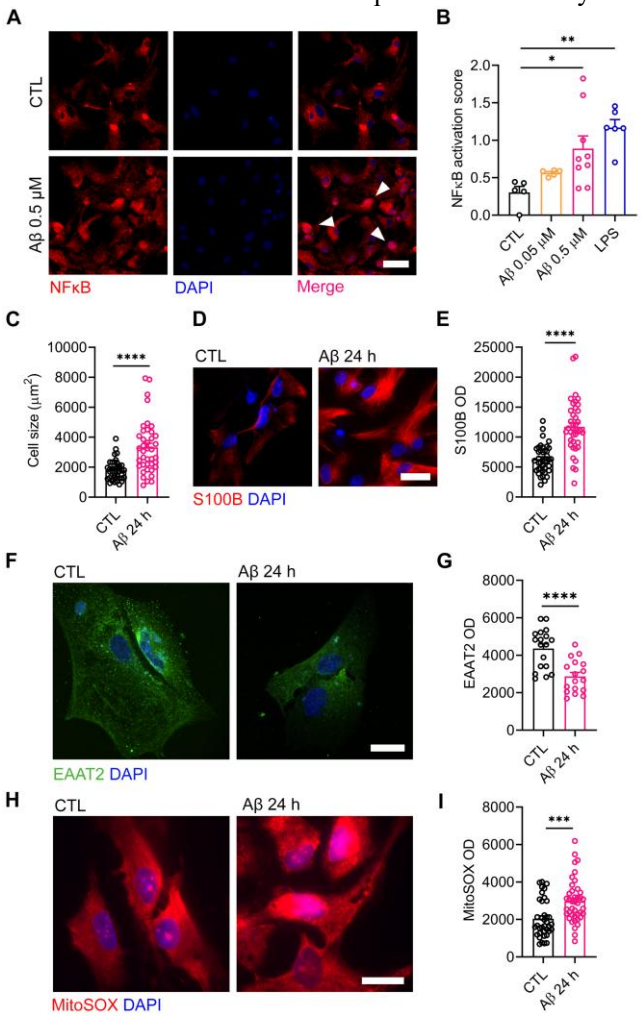

Figure 3. Amyloid-treated astrocytes show increased reactivity, oxidative stress and loss of glutamate transporters. (A) Immunofluorescence for p65 NFκB in primary astrocytes exposed to 0.5 µM Aβ for 90 minutes. Arrowheads indicate cells with high NFκB nuclear translocation. **(B)** Activation score based on NFκB nuclear translocation in primary astrocytes incubated in control media (CTL), 0.05 µM Aβ, 0.5 µM Aβ or LPS as a positive control (Kruskal-Wallis test; Holm-Sidak's test; *p<0.05, **p<0.01; n per group CTL=5, Aβ 0.05 µM=5, Aβ 0.5 µM=9, LPS=6;the n corresponds to confocal fields per condition from at least 2 cell culture technical replicates). **(C)** Quantification of mean cell size under control conditions or incubated with amyloid for 24 h in differential interference contrast (DIC) images (Student's *t* test; ****p<0.001; n per condition=40). **(D)** Immunofluorescence for S100B in primary astrocytes incubated with 0.5 µM Aβ for 24 h. **(E)** Quantification of S100B optical density (OD) in primary astrocytes (Student's *t* test; ****p<0.001; n per condition=40). **(F)** Immunofluorescence for glutamate transporter EAAT2 in control and Aβ- exposed astrocytes. **(G)** Quantification of EAAT2 optical density in control and Aβ-exposed astrocytes (24 h incubation time; Student's *t* test; **p<0.01; n per condition CTL=18, Aβ=17). **(H)** MitoSOX staining in control and Aβ- exposed primary astrocytes. **(I)** Quantification of MitoSOX optical density primary astrocytes (Student's *t* test; ***p<0.005; n per condition CTL=37, Aβ=41). Scale bars=20 µm for all images. All cells were counterstained with DAPI (blue). The n in C-I corresponds to cells per condition from at least 2 cell culture technical replicates. All the data are expressed as the means ± SEMs.

Astrocytes respond to amyloid beta in vitro with proinflammatory activation, oxidative stress and loss of glutamate transporters

To test whether mouse astrocytes *in vitro* adopted similar activation phenotypes in response to amyloid β (Aβ) as those seen in the *in vivo* model of AD-like amyloid pathology, we used a primary culture protocol. Mouse primary astrocytes were exposed to 0.05 or 0.5 µM Aβ peptides in fibrillary form for 90 minutes to determine the pro-inflammatory activation with p65 NFκB immunostaining (Fig. 3A-B). Amyloid β exposure was associated with a higher NFκB nuclear translocation than control astrocytes at the 0.5 µM concentration (CTL vs. 0.5 µM Aβ, $p<0.05$, one-way ANOVA, Holm-Sidak's test). Incubation with lipopolysaccharide (LPS) was used as a positive control. Also, astrocytes exposed to 0.5 µM Aβ for 24 h showed an increased cell size ($p<0.001$, Student's t test; Fig. 3C) and higher S100B optical density ($p<0.001$, Student's t test; Fig. 3D-E) than control cells. Concomitantly, glutamate transporter EAAT2 was decreased in Aβ- exposed astrocytes ($p<0.001$, Student's t-test; Fig. 3F-G) indicating a loss of homeostatic functions. This phenotype was accompanied by increased oxidative stress evidenced by higher MitoSOX optical density in amyloid-treated astrocytes than in control cells. ($p<0.005$, Student's t test; Fig. 3H-I). These results indicate that amyloid peptides induce an astrocyte profile that comprises pro-inflammatory reactivity and concurrent loss of pro-homeostatic characteristics.

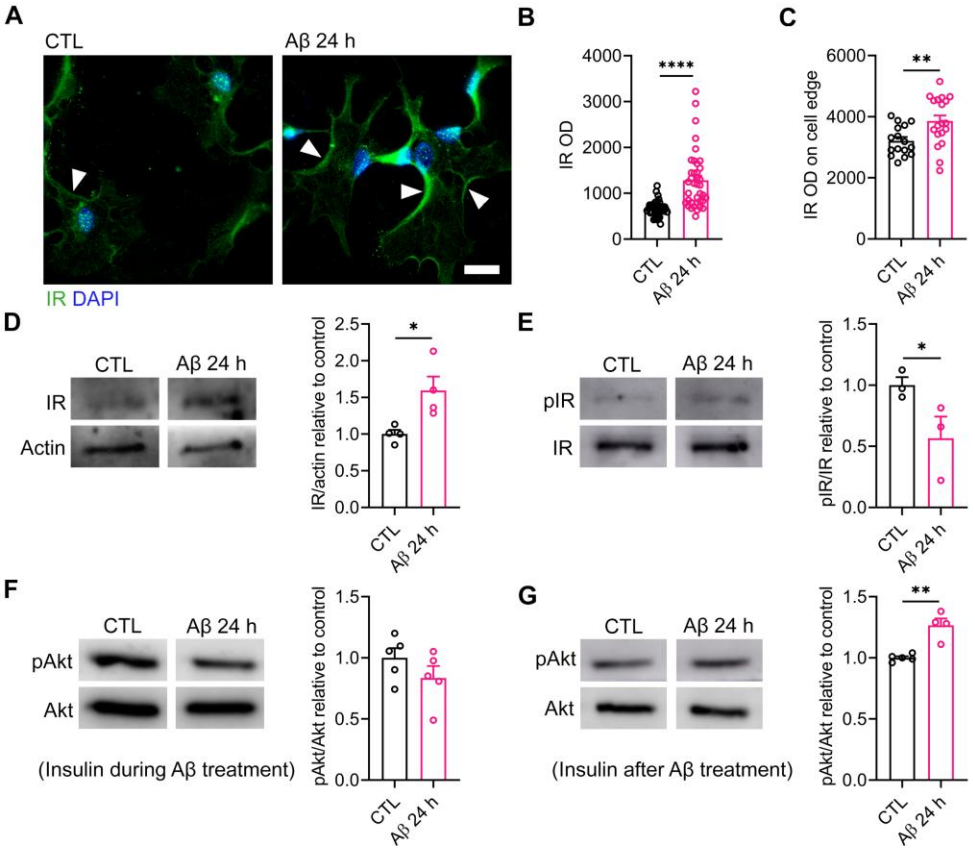

Figure 4. Astrocytes exposed to amyloid peptides showed higher levels and membrane localization of the insulin receptor but presented deficits in insulin signaling. **(A)** Representative confocal images of primary mouse astrocytes exposed to control medium (CTL) or fibrilized Aβ for 24 h, immunostained for insulin receptor (IR; green) and counterstained with DAPI (blue). Arrowheads indicate IR concentrated in the edge of cells. Scale bar=20 µm. **(B-C)** Quantification of IR optical density in the whole cell (B) and in cell edges (C; two-tailed Student's *t* test; **p<0.01, ****p<0.001; n for IR OD=38 per condition; n for IR OD in cell edge CTL=16, Aβ=19; the n corresponds to confocal fields per condition from at least 2 cell culture technical replicates). **(D)** Immunoblot for IR and actin in astrocytes after 24 h Aβ exposure (Mann Whitney test; *p<0.05; n=4 per group). **(E)** Immunoblot for pIR (phospho Y1361) and IR in astrocytes after an insulin stimulus during the final 2 h of the protocol (Mann Whitney test; *p<0.05; n=3 per group). **(F)** Immunoblot for pAkt (phospho S473) and Akt in astrocytes after an insulin stimulus during the final 2 h of the protocol (Mann Whitney test p=0.111; n=4 per group). **(G)** Immunoblot for pAkt and Akt in astrocytes exposed to an insulin stimulus for 2 h after the end of amyloid incubation (Mann Whitney test; *p<0.05; n=3 per group). Ratios shown in panels D-G are relativized to the CTL group. The n in D-G corresponds to cell culture technical replicates per condition. All the data are expressed as the means ± SEMs.

In vitro exposure to Aβ increases IR levels but impairs insulin signaling in astrocytes

To further characterize the astrocytic phenotype induced by amyloid peptides, we evaluated parameters related to the insulin signaling pathway. Exposure of astrocytes to 0.5 μM Aβ for 24 h induced increased IR positive signal ($p<0.001$, Student's t test; Fig. 4A-B), higher localization of the receptor in the edge of cells ($p<0.01$, Student's t test; Fig. 4C) and augmented IR levels by immunoblot ($p<0.05$, Student's t test; Fig. 4D; complete blots for Figure 4 are presented in Supplementary Fig. 8) compared with control astrocytes. Then, to test the functionality of the insulin signaling pathway, we analyzed the phosphorylation of IR (phospho Y136) and downstream Akt (phospho S473) after an insulin stimulus during the last 2 hours of amyloid incubation. This insulin scheme was sufficient to stimulate downstream signaling inducing the phosphorylation of Akt in control astrocytes (Supplementary Fig. 9). Even though IR levels were increased in amyloid treated cells, insulin-induced IR phosphorylation was lower than in control cells ($p<0.05$, Student's t test; Fig. 4E), while Akt phosphorylation remained unchanged (Fig. 4F). This could indicate impaired astrocytic insulin signaling or interference with binding of the hormone to its receptor. Accordingly, Aβ colocalized with IR both at the edge of the cells and at the soma (Supplementary Fig. 10). In this sense, if Aβ was removed by changing culture media before the insulin stimulus, Akt phosphorylation was increased compared to control astrocytes ($p<0.05$, Student's t test; Fig. 4G), possibly connected to amyloid unbinding from IR along with increased IR levels.

In vitro exposure of astrocytes to Aβ enhances glucose uptake and lactate release. Role of insulin

Given the alterations found in the insulin pathway in Aβ-exposed astrocytes, we sought to evaluate astrocytic glucose metabolism and its potential regulation by insulin. Glucose uptake was evaluated using the fluorescent probe 2-NBDG and measuring the cellular signal by fluorometry and Incucyte imaging. Astrocytes were incubated with Aβ for 2 h or 24 h to compare the initial and the sustained response to the amyloid insult, respectively. At both amyloid exposure times we found an increased 2-NBDG signal measured in a fluorometer (Aβ 2 h vs. CTL, $p<0.05$, one-way ANOVA, Sidak's test; Fig. 5A) and in the Incucyte live-cell analysis system (Aβ 24 h vs. CTL, $p<0.05$, one-way ANOVA, Sidak's test; Fig. 5B-C). Applying insulin during the last hour of Aβ incubation reversed the increase in glucose uptake at both exposure times (Aβ 2 h vs. Aβ 2 h + insulin $p<0.05$, Aβ 24 h vs. Aβ 24 h + insulin $p<0.01$). To test if insulin effect was dependent on its action on insulin receptor (IR) or the IGF1 receptor (IGF1R), we co-treated cells with BMS-536924 (IR/IGF1R inhibitor) or NVP-ADW742 (IGF1R inhibitor). We speculate that insulin effect was dependent on IR functionality as it was prevented by the IR/IGF1R inhibitor (Aβ 24 h + insulin vs. Aβ 24 h + insulin + BMS $p<0.001$; Fig. 5C) but not by the IGF1R specific inhibitor (Supplementary Fig. 11). Also, astrocytes incubated for 24 h with Aβ showed an increased presence of the glucose transporter GLUT1 in the edge of the cell profile (CTL vs. Aβ 24 h, $p<0.005$, one-way ANOVA, Tukey's test), an effect that was reversed when insulin was added in the last hour of the protocol (Aβ 24 h vs. Aβ 24 h + insulin, $p<0.001$; Fig. 5D-E).

Then, we evaluated the effect of lactate release by a colorimetric method in two different culture conditions, under high-glucose (17.5 mM) DMEM/F12 media or under low-glucose (5.5 mM; closer to physiological glucose levels) Earle's buffer. The aim of this protocol was to evidence possible differences in the astrocytic response to the nutrient excess or scarcity. Under the low glucose/low nutrients condition, exposure to Aβ initially stimulated lactate release (CTL vs. Aβ 2 h, $p<0.05$, one-way ANOVA, Sidak's test) but this effect was lost at the 24 h setting (Fig. 5F), suggesting a time-dependent response to glucose/nutrients scarcity.

Additionally, the effect was also lost under high glucose/nutrients availability (DMEM/F12 medium with 17.5 mM glucose) as Aβ did not stimulate lactate release neither at the 2 h nor at the 24 h incubation times (Fig. 5G), suggesting a context-dependent response, as well. Interestingly, glycogen content was increased in astrocytes incubated in a low glucose/low nutrients medium (*$p<0.05$, one-way ANOVA, Sidak's test; Fig. 5H-I) both at 2 h and 24 h amyloid incubation times. This could suggest a paradoxical effect for amyloid enhancing glycogen storage and, simultaneously, lactate release under a low glucose/low nutrients context. Incubation with amyloid in the high glucose/high nutrients medium did not modify glycogen storages compared to control cells (Fig. 5J), indicating, as seen for lactate secretion, a lack of effect of amyloid under glucose/nutrient abundance.

Amyloid beta (Aβ) alters mitochondrial morphology, function, and metabolism in primary mouse astrocytes. Role of insulin on amyloid internalization and mitochondrial functionality

One of the crucial homeostatic functions of astrocytes is the capacity to internalize Aβ from the extracellular space. Given that the phagocytic and catabolic capacity of astrocytes depends on insulin signaling [34, 35], we sought to evaluate if a short insulin treatment was able to

regulate the intracellular amyloid content in primary mouse astrocytes. Astrocytes incubated for 24 h with 0.05 µM Aβ were treated with insulin at 0.1 or 1 µM concentrations during the last hour. We performed immunofluorescence using the 4G8 antibody to detect Aβ and found an effect of 1 µM insulin increasing intracellular amyloid (Aβ vs. Aβ + 1 µM insulin, $p<0.05$, one-way ANOVA, Sidak's test; Fig. 6A-B), probably due to increased internalization. A significant fraction of the intracellular Aβ colocalized with LC3+ vesicles (Supplementary Fig. 12), indicating a role for autophagy in astroglial amyloid metabolism as previously reported [28].

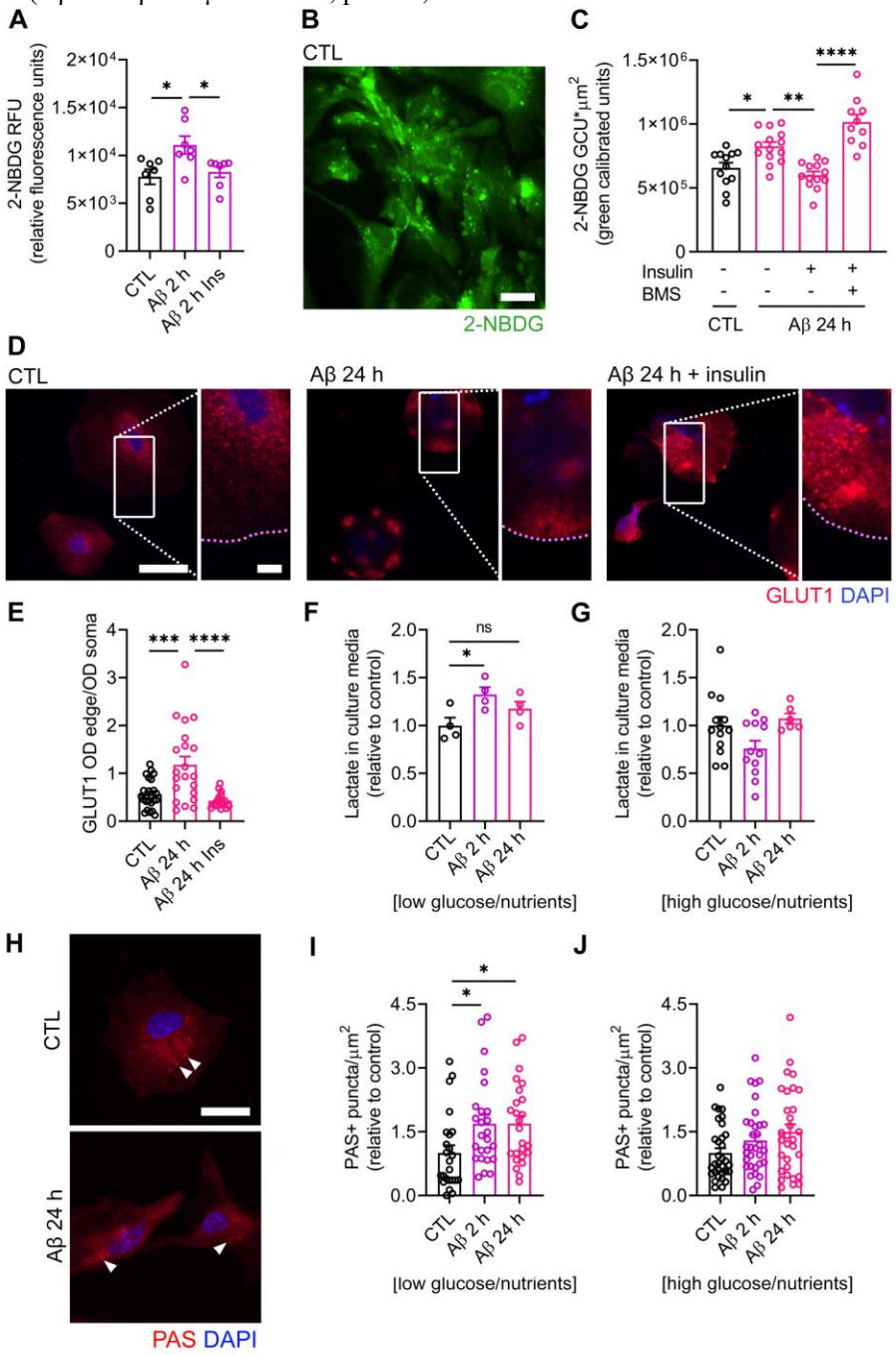

Figure 5. Amyloid increased astrocytic glucose uptake and GLUT1 membrane localization while insulin reversed these effects. Lactate release stimulated by amyloid peptides was dependent on glucose availability. (A) Fluorometer quantification of 2-NBDG uptake in primary astrocytes incubated for 2 h with 0.5 Aβ and insulin for the last hour (Relative fluorescence units=RFU; one-way ANOVA; Sidak's test, *$p<0.05$; n=7 technical replicates/group from primary culture preparations from 8 mouse pups). **(B)** Incucyte imaging of 2-NBDG uptake in

primary astrocytes (scale bar=10 µm). **C**. Quantification of 2-NBDG uptake in astrocytes exposed to Aβ for 24 h in the presence or absence of insulin and/or the IR/IGF1R inhibitor BMS during the last hour (green calibrated units=GCU*µm^2; one-way ANOVA; Sidak's test, **p<0.01, ****p<0.001; n per condition CTL=12, Aβ=14, Aβ+ins=13, Aβ+ins+BMS=10; the n corresponds to Incucyte fields from at least 2 cell culture technical replicates). **(D)** Representative confocal images from GLUT1 (red) immunofluorescence (DAPI counterstain in blue) in astrocytes exposed to Aβ for 24 h in the presence or absence of insulin for the last hour. Pink dotted lines in the insets indicate the edge of cells (scale bars=50 and 10 µm for large field and inset, respectively). **(E)** Quantification of the GLUT1 cell edge OD / cell soma OD ratio (One-way ANOVA; Tukey's test, ***p<0.005, ****p<0.001; n per group CTL=24, Aβ=22, Aβ+ins=18; the n corresponds to confocal fields from at least 2 cell culture technical replicates). **(F)** Lactate release (absorbance) collected during 1 h after the incubation with Aβ for 2 h or 24 h in a 5.5 mM glucose Earle's buffer (low glucose/low nutrients; One-way ANOVA; Sidak's test, *p<0.05; n=4 per group; the n corresponds to technical replicates/group from primary culture preparations). **(G)** Lactate release (absorbance) collected during the last 2 h of an incubation with Aβ for 2 h or 24 h in a 17.5 µM glucose DMEM/F12 medium (n per group CTL=13, Aβ 2h=12, Aβ 24h=6 technical replicates/group from primary culture preparations). Lactate levels were relativized to the corresponding CTL group. **(H)** Confocal images for astrocytes stained with PAS to evaluate glycogen storage (DAPI counterstain in blue) under control conditions or incubated with Aβ for 24 h (scale bar=50 µm). **(I-J)** Density of PAS+ puncta /µm2 (relativized to the corresponding CTL group) in astrocytes exposed to Aβ for 2 h or 24 h in a 5.5 mM glucose Earle's buffer (I) or 17.5 mM glucose DMEM/F12 (J; One-way ANOVA; Sidak's test, *p<0.05; n=24-30 cells per group from at least 2 cell culture technical replicates). All the data are expressed as the means ± SEMs.

In order to further characterize the homeostatic function of astrocytes under amyloid incubation, we evaluated parameters related to mitochondrial health. First, we stained astrocytes with the MitoSpy probe to assess the total mitochondrial mass (Fig. 6C). After a 24-h Aβ exposure, astroglial optical density of MitoSpy was decreased (p<0.001, Student's t test; Fig. 6D) while the average size of mitochondria remained unchanged (Fig. 6E). To evaluate mitochondrial functionality, we stained astrocytes with the MitoTracker Red probe, which signal is proportional to the integrity of the mitochondrial membrane potential (Fig. 6F). Amyloid β treatment was associated with a decrease in the size and an increase in the number of MitoTracker+ mitochondria (CTL vs. Aβ 24 h, p<0.001, one-way ANOVA, Sidak's test; Fig. 6G-H), suggesting a lower and fragmented functional area. In the same sense, MitoTracker optical density decreased in amyloid-treated astrocytes indicating defective membrane potential (CTL vs. Aβ 24 h, p<0.005, one-way ANOVA, Sidak's test Fig. 6I). Even though insulin did not correct the changes in size and number of MitoTracker+ mitochondria, it was able to restore MitoTracker staining intensity (p<0.001), a proxy for the recovery of mitochondrial membrane potential.

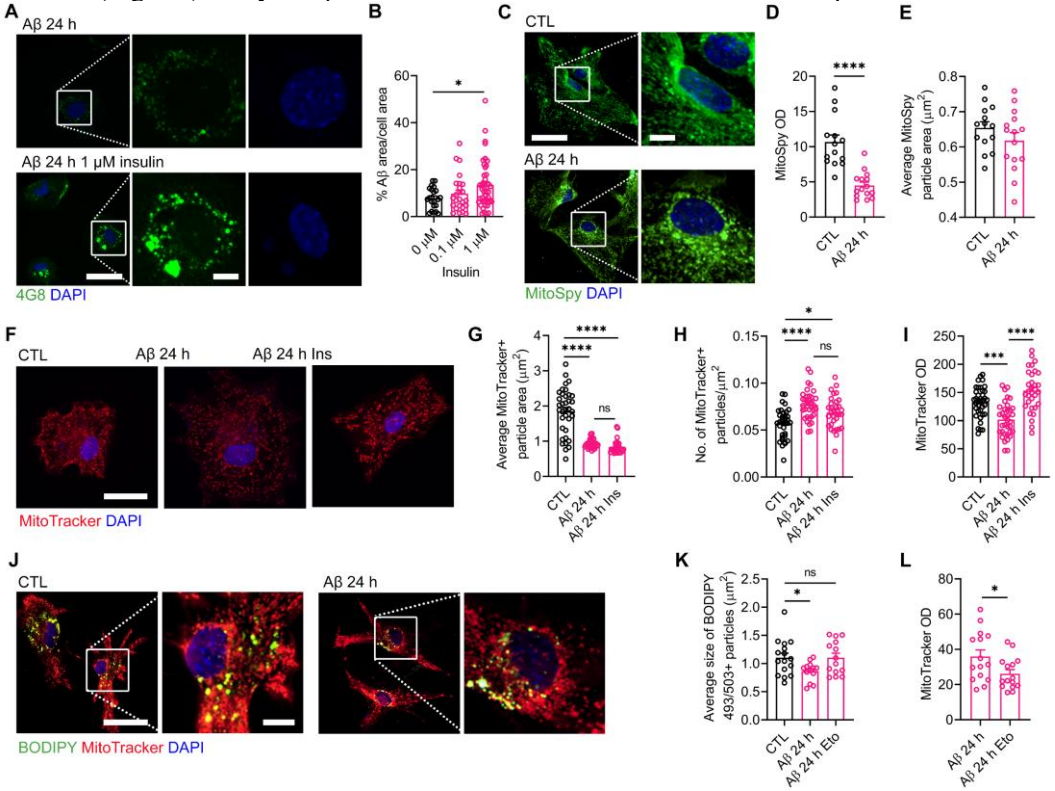

Figure 6. Amyloid treatment induced mitochondrial and metabolic disturbances in Aβ-treated astrocytes. Insulin increased amyloid uptake and recovered mitochondrial membrane potential. (A) Representative confocal images of astrocytes incubated with 0.5 µM Aβ for 24 h and insulin at 0, 0.1 or 1 µM concentrations for 1 h and immunostained with the 4G8 antibody for Aβ (green). **(B)** Quantification of the percentage of cell area occupied by the 4G8 immunostaining (One-way ANOVA, Sidak's test, *p<0.05). Scale bars=50 and 10 µm for large fields and insets, respectively. **(C)** Confocal images of MitoSpy-stained astrocytes (green). Scale bars= 50 and 10 µm for large fields and insets, respectively. **(D-E)** Quantification of optical density (D) and average size of mitochondria (E) in MitoSpy-stained astrocytes incubated with control (CTL) media or 0.5 µM Aβ for 24 h (Student's t test, ****p<0.001). **(F)** Confocal images of astrocytes stained with the MitoTracker probe (red). Scale bar=30 µm. **(G-I)** Quantification of the average size (G), density of mitochondria (H) and mean optical density (I) in MitoTracker-stained astrocytes incubated with control media, 24-h Aβ or 24-h Aβ and 1-h 1 µM insulin (One-way ANOVA, Sidak's test, *p<0.05, ***p<0.005, ****p<0.001; n=35 cells per condition). **(J)** Confocal images of astrocytes stained with MitoTracker (red) and BODIPY 493/503 (green) probes. Scale bars= 50 and 20 µm for large fields and insets, respectively. **(K)** Optical density of the BODIPY probe under control condition or Aβ for 24 h with or without the CPT1 inhibitor etomoxir (One-way ANOVA, Sidak's test, ***p<0.005). **(L)** Optical density of the MitoTracker probe in astrocytes incubated with Aβ for 24 h with or without etomoxir (Student's *t* test, *p<0.05; n=15 cells per condition). All cells were counterstained with DAPI (blue).

As astrocytes also rely on the β oxidation of fatty acids for energy production, we analyzed the lipid storages after amyloid exposure. After 24 h of Aβ exposure astrocytes showed a decrease in the size of lipid droplets stained with the BODIPY 493/503 probe (CTL vs. Aβ 24 h, p<0.05, one-way ANOVA, Sidak's test; Fig. 6J-K). This effect was lost when the transport of fatty acids to the mitochondria was inhibited with the carnitine palmitoyltransferase I (CPT I) inhibitor etomoxir, suggesting that amyloid was associated with increased usage of fatty acid. To test if the smaller size of lipid droplets related to Aβ exposure was associated with induced fatty acid oxidation, we analyzed the effect of etomoxir on the mitochondrial membrane potential. After 24 h of Aβ exposure, MitoTracker optical density was decreased in astrocytes co-treated with etomoxir (Aβ vs. Aβ + etomoxir, p<0.05, Student's t test; Fig. 6L), indicating that the maintenance of mitochondrial membrane potential depended, at least partially, on fatty acid β oxidation. As a control of potential etomoxir toxicity on mitochondria, control cells were incubated with the inhibitor, and no differences were found in the MitoTracker optical density with that of vehicle-treated cells (Supplementary Fig. 13).

DISCUSSION

In this report, we have demonstrated that experimental amyloid pathology is accompanied by concurrent metabolic and glial responses that could have a role in AD pathophysiology.

Insulin resistance and Alzheimer's disease

Although most of the metabolic changes found in AD models are usually linked to a peripheral insulin-resistance profile with hyperglycemia [36–40], they diverge with the normoglycemic phenotype that we describe. We show here that adult PDAPP-J20 transgenic (Tg) mice modelling AD suffered a relatively minor peripheral metabolic change. While hepatic Akt phosphorylation after insulin stimulation was unaffected in Tg mice, circulating insulin levels were increased compared with control mice. In the context of normoglycemia this metabolic phenotype could comprise a subtle indicator of aberrant energy signaling and may be a consequence of hippocampal insulin resistance [7, 41]. This model carries the human APP gene with familial AD mutations that do not exert a direct role on systemic metabolism, reinforcing a role for the hippocampal insulin dysregulation. Even though pancreatic expression of inflammatory markers was not increased in Tg mice, we cannot discard future pancreatic damage due to insulin overproduction and a direct effect of amyloid on β-cells [42].

Brain insulin resistance is usually associated with glucose hypometabolism and a subsequent impaired energy supply for neurons [3, 43]. Reinforcing this concept, genetic ablation of hippocampal IR is associated with memory and neuroplasticity defects [44]. Accordingly, we found a hippocampal-dependent memory impairment and an anxiety-like behavior in Tg mice, confirming functional deficits in this AD model [28, 29, 45].

Several mechanisms can contribute to the reduced response to insulin, including downregulation of insulin receptors, impaired binding of insulin to its receptors, and/or the abnormal activation of the insulin signaling cascade [46]. Under conditions of chronic hyperinsulinemia, brain insulin receptors are usually downregulated, leading to central insulin resistance and deficits in glucose availability [32]. We found decreased levels of IR in the hippocampus of Tg mice in comparison with control mice, both in the whole tissue and in

astrocytes. Regarding insulin sensitivity, we identified a sex-dependent response, i.e. a decrease in the phosphorylation of hippocampal Akt upon insulin stimulation in male Tg mice. Conversely, female Tg mice showed normal Akt phosphorylation. As the pathology may not progress equivalently in male and female AD patients and animal models [47, 48], a more thorough comparison of sex- and age-dependent changes should be done in future research. Sex hormones, particularly estrogens, may contribute to these differences, as estradiol has been shown to modulate insulin signaling and exert neuroprotective effects in models of neurodegeneration and aging [49, 50].

In addition to the mechanisms discussed above, other upstream regulators may also contribute to central insulin resistance in AD. The suppressor of cytokine signaling 3 (SOCS3) -a known inhibitor of insulin signaling- has been found upregulated in the brains of AD patients, particularly in regions with high Aβ deposition [51]. This increase suggests that SOCS3 could block insulin receptor signaling in the AD brain. Similarly, the phosphatase PTP1B, which dephosphorylates and inactivates the insulin receptor, has been linked to defective insulin signaling in neurons from AD models [52]. Preclinical studies have shown that pharmacological inhibition of PTP1B reduces microglial activation and improves insulin signaling in the brain, supporting its potential relevance in AD pathophysiology [53]. Together, these findings suggest that SOCS3 and PTP1B may represent promising therapeutic targets in AD.

Astroglial activation and insulin signaling

In our study, hippocampal astrocytes showed morphological signs of reactivity like higher GFAP area and increased levels of S100B. In parallel, mouse primary astrocytes responded to Aβ exposure with increased NFkB nuclear translocation and increased S100B expression, indicating a proinflammatory activation profile in these *in vitro* conditions. This was accompanied by higher levels of reactive oxygen species evidenced by the MitoSOX probe.

The proinflammatory astroglial activation not only correlates with an increase in damage signals, but can also affect the basic metabolic and energetic homeostatic functions of the nervous system. Interestingly, astroglial inflammatory activation was coupled to a loss of the EAAT2 glutamate transporter, an event that could increase neuronal vulnerability to glutamate toxicity [54]. Chronic loss of this transporter has been associated with impaired insulin signaling in the brain of AβPPSwe/PS1ΔE9 mice along with decreased phosphorylation of IR [55] as we describe here. Impaired insulin signaling in astrocytes could exacerbate AD-like pathology, leading to cognitive deficits, increased Aβ burden, and neuroinflammation, as demonstrated in other AD models [21]. In a vicious cycle-like manner, insulin resistance in the context of AD can increase APP and Aβ levels while amyloid peptides can directly bind to IR and preclude insulin signaling [56, 57]. Also, De Felice et al. have demonstrated that amyloid oligomers are able to remove insulin receptors from the neuronal surface and promote their internalization [58], underscoring the interactions between Aβ and IR.

Regarding the potential effects of insulin on astroglial proinflammatory activation, signaling through the activation of the PI3K/Akt pathway can inhibit NF-κB nuclear translocation by suppressing the IKK complex [59]. However, under conditions of impaired insulin signaling, such as metabolic stress or exposure to proinflammatory stimuli like Aβ or cytokines, NF-κB activation is enhanced, leading to increased astrocyte reactivity [60]. This bidirectional crosstalk is central to the interplay between metabolic and inflammatory signaling in the CNS.

In mouse primary astrocytes we found increased levels of IR after amyloid exposure. However, phosphorylation of this receptor was dampened, indicating impaired insulin signaling in response to amyloid. Interestingly, if amyloid was removed before insulin incubation the phosphorylation of Akt was increased, suggesting a competitive effect of amyloid on IR and an over response possibly due to the increased levels of IR. This could represent an attempt to overcome the defects in insulin signaling in the context of amyloid acute exposure.

The upregulation of IR signaling seen in our *in vitro* experiments possibly reflects an early, cell-autonomous compensatory response to acute amyloid stress. In this simplified system, astrocytes are isolated from other brain cell types and thus do not experience the complex cellular interactions and signaling present *in vivo*. Conversely, the downregulation of IR observed in the PDAPP-J20 mice after 8 months of amyloid pathology represents a chronic, integrated response within the brain's multicellular environment, including neurons, microglia, and vascular cells. This prolonged exposure likely triggers more complex regulatory feedback mechanisms and neuroinflammatory processes, resulting in diminished IR expression and signaling.

Astroglial glucose metabolism in AD

Neuroinflammation and glial activation, as in AD, are frequently accompanied by metabolic alterations. Reactive astrocytes can display higher glucose consumption and lactate release [61, 62] as described here. Astrocytes incubated with Aβ showed increased

glucose uptake, upregulated GLUT1 glucose transporter and larger glycogen reserves, in line with the inflammatory activation mentioned before. Also, Aβ stimulated lactate release at the 2 h incubation time under low glucose/nutrients availability. However, this effect was lost under high glucose/nutrient availability (17.5 mM) or at longer incubation times indicating a context- and time-dependent metabolic response. These results suggest that, initially, amyloid may act as a short-term signal improving lactate availability and potentially aiding neuronal survival, but at longer times, as in AD, or under excess glucose and nutrients can lead to a metabolic deficit as previously suggested [2, 63]. In the same sense, in a recent publication Elsworthy et al. have shown that iPSC-derived astrocytes from familial AD patients display more marked metabolic deficits and gliosis than control astrocytes acutely exposed to Aβ [64], confirming a context- and time-dependent response.

On the other hand, and even though lactate is considered a main fuel for neurons, excess lactate release by astrocytes could be detrimental. Regional brain lactate levels, as a proxy of neuronal activity, have been shown to be associated with local amyloid levels [65] suggesting that increased glycolysis in the context of AD can potentiate amyloid pathogenic effects. Longitudinal studies of autosomal AD patients suggest that astrogliosis and increased glucose metabolism are early events that precede in many years the onset of overt amyloid pathology and cognitive impairment [66, 67]. As the disease progresses, astrogliosis diminishes and glucose metabolism declines [68], suggesting a concurrent response and a significant and biphasic patho-physiological role for astrocytes.

Effects of insulin on astroglial glucose metabolism

Astrocytic insulin signaling is crucial for mitochondrial function and cognitive processes such as working memory [69]. However, insulin action on the regulation of astroglial glucose uptake is not clear as both insulin-sensitive and insulin-insensitive glucose transporters coexist in these cells. Insulin exposure reversed the increase in astrocyte glucose uptake after Aβ incubation, and this effect was dependent on IR functionality. These results are coherent with evidence showing that IR and IGF1R reductions affect glucose uptake by astrocytes both *in vivo* [70, 71] and *in vitro* [69]. In line with this, we found increased GLUT1 levels in amyloid-treated astrocytes and a reversion by insulin. However, there is no consensus regarding this regulation. Using a nanosensor-based approach, Muhič et al. did not find effects of insulin or IGF1 on glucose transport in rat astrocytes *in vitro* [72]. Even though the most abundant astrocytic glucose transporters GLUT1 and GLUT3 are not sensitive to insulin in terms of glucose transport, mechanisms involving the subcellular re-localization of these transporters could be a part of insulin and IGF1 actions and play a role in AD [73]. Moreover, IR reductions at the vascular level could affect brain glucose uptake in AD as shown by Leclerc et al. both in human postmortem samples and in 3xTGAD mice [74]. In our *in vitro* model we found upregulated astroglial IR in response to amyloid exposure, in line with increased glucose uptake and lactate release. However, in the *in vivo* model, more representative of a chronic scenario, transgenic mice astrocytes showed lowered IR levels. Along with the impaired insulin signaling found *in vivo*, loss of astrocytic IR exacerbates the pathological phenotype in 5xTGAD mice [21], indicating the existence of a vicious cycle that aggravates the disease.

Insulin action on astroglial amyloid content and energy metabolism

Insulin treatment was associated with an increased amyloid content in mouse primary astrocytes. The regulation that insulin signaling exerts on phagocytosis and catabolism, as has been reported in primary astrocytes [34, 35], could underlie this effect. Amyloid exposure disrupted astroglial mitochondrial membrane potential, highlighting a shift in metabolic dynamics and mitochondrial functionality in response to Aβ, consistent with recent insights into metabolic adaptation [75]. However, these dynamics may differ between human and mouse brains. Human astrocytes exposed to $A\beta_{1-42}$ show initial mitochondrial fusion followed by excessive fission and a shift to peroxisomal oxidation of fatty acids [76], probably affecting brain energetic homeostasis. Glucose metabolism is slower and respiration is better coupled in the human cortex compared with the mouse cortex, probably indicating a more efficient mitochondrial function [77]. Even though insulin did not reverse decreased size and increased numbers of mitochondria in amyloid-treated astrocytes, it was able to restore membrane potential. Interestingly after amyloid exposure, astroglial mitochondria showed enhanced fatty acid β-oxidation, as suggested by the decrease in LDs density and the observation of a decreased membrane potential when the transfer of fatty acids was prevented through inhibition of CPT1. There is evidence that astrocytes with impaired insulin signaling have increased fatty acid β-oxidation associated with an upregulation of CPT1c [70] and with more oxygen consumption [78], as a probably inefficient mechanism to meet neuronal energy needs. A quantitative analysis of CPT1 and related key enzymes would strengthen our results regarding this amyloid-associated metabolic shift.

Our observation that Aβ reduces lipid storage in serum-starved astrocytes likely reflects the short duration of exposure in our assay, capturing early metabolic responses. In contrast, studies reporting Aβ-induced LDs accumulation often involve longer exposure times or chronic conditions, during which LDs progressively accumulate near mitochondria as a protective or pathological response. Moreover, nutrient availability and metabolic phase critically influence LDs dynamics [79]. Under serum starvation, cells may mobilize lipid stores differently, and acute Aβ exposure might initially promote lipid consumption before later inducing LD formation as part of a stress adaptation process [80].

Our results from the *in vitro* model showing a rescue of membrane potential and increased amyloid uptake with insulin treatment should be correlated with in vivo evidence for the neuroprotective effects of insulin. In 3xTg-AD mice, Chen et al. have shown that 7-day intranasal insulin restored brain insulin signaling, increased synaptic proteins, reduced Aβ40 levels, and suppressed microglial activation [81]. In APPswe/PS1dE9 mice, a 6-week insulin treatment improved cognition, enhanced brain insulin signaling, reduced amyloid pathology and promoted hippocampal neurogenesis [82]. While preclinical evidence supports insulin's benefits for mitochondrial/neuronal health, large-scale clinical trials lack consistent cognitive/functional improvements. Ongoing studies focused on combination therapies and delivery optimization should be done to confirm insulin therapeutic potential in AD.

Limitations of this study

The main limitation of this study and of those studying age-associated diseases like AD is the narrow time window that encompass mouse models and cell cultures. Ideally, multiple time points should be evaluated in further studies to better characterize the dynamic nature of the brain and astroglial metabolic changes that develop during AD progression. Also, the effects found with the pharmacological agonists and inhibitors of the pathways studied here should be complemented with genetic tools to confirm mechanistic hypotheses. Regarding the mouse model of AD that we used here it is important to note that it does not reflect the tau pathology that occurs in AD, at least at this time frame. However, our primary objective was to investigate the effects of amyloid pathology specifically and we believe that the PDAPP-J20 model is well-suited for this purpose, as it recapitulates amyloid accumulation and related synaptic and cognitive deficits. Future studies may indeed benefit from including tau pathology models to explore additional facets of AD-associated insulin resistance.

Concerning the in vitro model, our results show the response of mouse astrocytes and may not accurately demonstrate the behavior of human astrocytes. In addition, amyloid pathology *in vitro* was modelized using fibrilized amyloid peptides in a preparation that also contains a small fraction of peptides in soluble form. Amyloid preparation protocols can influence fibril morphology and aggregation state, potentially affecting biological activity and experimental outcomes [83]. Regarding concentration, we selected doses within ranges reported in the literature to balance the physiological relevance and the detectability of cellular responses [84], acknowledging that supraphysiological concentrations may induce non-specific effects [85]. A more complex protocol should be done in future research to analyze the differential effect of amyloid peptides in varying states of aggregation. In this study we have assessed mitochondrial dysfunction *via* the evaluation of the membrane potential and morphological parameters. Even though changes in mitochondrial membrane potential correlate with impaired ATP production and respiratory chain dysfunction in AD models [76], more comprehensive assays such as ATP quantification and real-time metabolic analysis would significantly strengthen our findings.

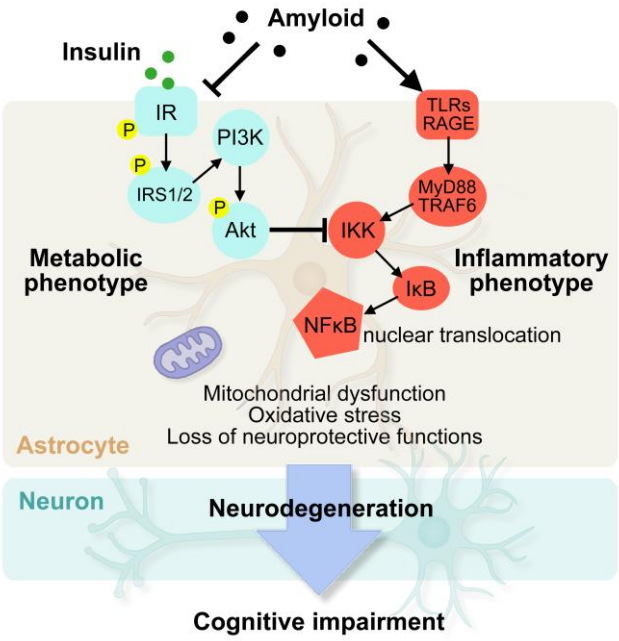

Figure 7. Working model. Experimental amyloid pathology induces concurrent metabolic and inflammatory astroglial responses, potentially influencing AD pathophysiology. Amyloid pathology can trigger both a metabolic phenotype, characterized by impaired insulin signaling, and an inflammatory phenotype, marked by oxidative stress and NFκB translocation in astrocytes. These phenotypes can interact, leading to a loss of neuroprotective functions, neurodegeneration, and ultimately, cognitive impairment.

Conclusion

Our findings highlight the interplay between glial metabolism, insulin signaling, and Aβ pathology in experimental AD progression (Fig. 7; working model). The shift in the astroglial metabolic profile could act as a link between the amyloid pathology and the loss of neuronal support that leads to neurodegeneration. Impaired brain insulin signaling may play a central role in the progression of the disease and the modulation of this pathway could represent a potential therapeutic avenue. However, as shown and discussed, the metabolic settings along the different stages of AD are variable and this variability could define the effectiveness of insulin-oriented treatments.

Acknowledgements

We thank Johnson & Johnson Argentina and Shirley Wenker for technical advice and reagents. Funding sources: Williams, Roemmers, René Barón, Bigand and IBYME Foundations, ANPCYT-FONCYT PICT Grants 2019-3692 (J.B.), 2019-3419 (F.S.), CONICET PIP Grant 2021-2023 #3125 (F.S.), CONICET fellowships (M. Bentivegna, A.G., J.P. and F.M.) and ANPCYT fellowships (M. Bellotto, N.G.P and J.P..). C.P., S.P.R., D.V., M.M.B., V.L.L., S.P.A., F.S. and J.B. are CONICET Career Researchers.

Author contributions

All the authors performed experiments. M. Bentivegna, C.P., S.P.A., F.S. and J.B. discussed the results and edited the manuscript. M. Bentivegna and J.B. conceived the study, analyzed the results, designed the Figures, performed statistical analyses and wrote the manuscript.

Competing interests

No conflicts of interest to declare.

Data and materials availability

Complete blots are shown in supplementary Figures. All the data is available upon reasonable request to the authors.

Supplementary Materials

The Supplementary data can be found online at: www.aginganddisease.org/EN/10.14336/AD.2025.0484.

References

[1] Alzheimer's Association Report (2023). 2023 Alzheimer's disease facts and Figures. Alzheimers Dement, 19:1598–1695.

[2] An Y, Varma VR, Varma S, Casanova R, Dammer E, Pletnikova O, et al. (2018). Evidence for brain glucose dysregulation in Alzheimer's disease. Alzheimers Dement, 14:318–329.

[3] Butterfield DA, Halliwell B (2019). Oxidative stress, dysfunctional glucose metabolism and Alzheimer disease. Nat Rev Neurosci, 20:148–160.

[4] Johnson ECB, Dammer EB, Duong DM, Ping L, Zhou M, Yin L, et al. (2020). Large-scale proteomic analysis of Alzheimer's disease brain and cerebrospinal fluid reveals early changes in energy metabolism associated with microglia and astrocyte activation. Nat Med, 26:769–780.

[5] Mullins RJ, Diehl TC, Chia CW, Kapogiannis D (2017). Insulin Resistance as a Link between Amyloid-Beta and Tau Pathologies in Alzheimer's Disease. Front Aging Neurosci, 9:118.

[6] Tong H, Capuano AW, Carmichael OT, Gwizdala KL, Bennett DA, Ahima RS, et al. (2023). Brain Insulin Signaling is Associated with Late-Life Cognitive Decline. Aging Dis. doi: 10.14336/AD.2023.1117.

[7] Biessels GJ, Reagan LP (2015). Hippocampal insulin resistance and cognitive dysfunction. Nat Rev Neurosci, 16:660–671.

[8] Di Domenico F, Lanzillotta C, Perluigi M (2024). Redox imbalance and metabolic defects in the context of Alzheimer disease. FEBS Letters, 1873-3468.14840.

[9] Sonntag K-C, Ryu W-I, Amirault KM, Healy RA, Siegel AJ, McPhie DL, et al. (2017). Late-onset Alzheimer's disease is associated with inherent changes in bioenergetics profiles. Sci Rep, 7:14038.

[10] Havrankova J, Roth J, Brownstein M (1978). Insulin receptors are widely distributed in the central nervous system of the rat. Nature, 272:827–829.

[11] Steen E, Terry BM, Rivera EJ, Cannon JL, Neely TR, Tavares R, et al. (2005). Impaired insulin and insulin-like growth factor expression and signaling mechanisms in Alzheimer's disease--is this type 3 diabetes? J Alzheimers Dis, 7:63–80.

[12] Corriveau-Lecavalier N, Adams JN, Fischer L, Molloy EN, Maass A (2024). Cerebral hyperactivation across the Alzheimer's disease pathological cascade. Brain Commun, 6:fcae376.

[13] Rae CD, Baur JA, Borges K, Dienel G, Díaz-García CM, Douglass SR, et al. (2024). Brain energy metabolism: A roadmap for future research. J Neurochem, 168:910–954.

[14] Cahoy JD, Emery B, Kaushal A, Foo LC, Zamanian JL, Christopherson KS, et al. (2008). A Transcriptome Database for Astrocytes, Neurons, and Oligodendrocytes: A New Resource for Understanding Brain Development and Function. J Neurosci, 28:264–278.

[15] Wang Q, Duan L, Li X, Wang Y, Guo W, Guan F, et al. (2022). Glucose Metabolism, Neural Cell Senescence and Alzheimer's Disease. IJMS, 23:4351.
[16] Magistretti PJ, Allaman I (2018). Lactate in the brain: from metabolic end-product to signalling molecule. Nat Rev Neurosci, 19:235–249.
[17] Lawrence JM, Schardien K, Wigdahl B, Nonnemacher MR (2023). Roles of neuropathology-associated reactive astrocytes: a systematic review. Acta Neuropathol Commun, 11:42.
[18] Rodríguez JJ, Olabarria M, Chvatal A, Verkhratsky A (2009). Astroglia in dementia and Alzheimer's disease. Cell Death Differ, 16:378–385.
[19] Fan L-Y, Yang J, Li M-L, Liu R-Y, Kong Y, Duan S-Y, et al. (2023). Single-nucleus transcriptional profiling uncovers the reprogrammed metabolism of astrocytes in Alzheimer's disease. Front Mol Neurosci, 16:1136398.
[20] Heni M (2024). The insulin resistant brain: impact on whole-body metabolism and body fat distribution. Diabetologia, 67:1181–1191.
[21] Chen W, Huang Q, Lazdon EK, Gomes A, Wong M, Stephens E, et al. (2023). Loss of insulin signaling in astrocytes exacerbates Alzheimer-like phenotypes in a 5xFAD mouse model. Proc Natl Acad Sci U S A, 120:e2220684120.
[22] Shen Z, Li Z-Y, Yu M-T, Tan K-L, Chen S (2023). Metabolic perspective of astrocyte dysfunction in Alzheimer's disease and type 2 diabetes brains. Biomedicine & Pharmacotherapy, 158:114206.
[23] Mucke L, Masliah E, Yu GQ, Mallory M, Rockenstein EM, Tatsuno G, et al. (2000). High-level neuronal expression of abeta 1-42 in wild-type human amyloid protein precursor transgenic mice: synaptotoxicity without plaque formation. J Neurosci, 20:4050–4058.
[24] Crispim Junior CF, Pederiva CN, Bose RC, Garcia VA, Lino-de-Oliveira C, Marino-Neto J (2012). ETHOWATCHER: validation of a tool for behavioral and video-tracking analysis in laboratory animals. Comput Biol Med, 42:257–264.
[25] McDonald DR, Brunden KR, Landreth GE (1997). Amyloid Fibrils Activate Tyrosine Kinase-Dependent Signaling and Superoxide Production in Microglia. J Neurosci, 17:2284–2294.
[26] Pomilio C, Gorojod RM, Riudavets M, Vinuesa A, Presa J, Gregosa A, et al. (2020). Microglial autophagy is impaired by prolonged exposure to β-amyloid peptides: evidence from experimental models and Alzheimer's disease patients. Geroscience, 42:613–632.
[27] Bolte S, Cordelières FP (2006). A guided tour into subcellular colocalization analysis in light microscopy. Journal of Microscopy, 224:213–232.
[28] Gregosa A, Vinuesa Á, Todero MF, Pomilio C, Rossi SP, Bentivegna M, et al. (2019). Periodic dietary restriction ameliorates amyloid pathology and cognitive impairment in PDAPP-J20 mice: Potential implication of glial autophagy. Neurobiol Dis, 132:104542.
[29] Beauquis J, Vinuesa A, Pomilio C, Pavía P, Galván V, Saravia F (2014). Neuronal and glial alterations, increased anxiety, and cognitive impairment before hippocampal amyloid deposition in PDAPP mice, model of Alzheimer's disease. Hippocampus, 24:257–269.
[30] Wright AL, Konen LM, Mockett BG, Morris GP, Singh A, Burbano LE, et al. (2023). The Q/R editing site of AMPA receptor GluA2 subunit acts as an epigenetic switch regulating dendritic spines, neurodegeneration and cognitive deficits in Alzheimer's disease. Mol Neurodegeneration, 18:65.
[31] Duarte AI, Santos P, Oliveira CR, Santos MS, Rego AC (2008). Insulin neuroprotection against oxidative stress is mediated by Akt and GSK-3β signaling pathways and changes in protein expression. Biochimica et Biophysica Acta (BBA) - Molecular Cell Research, 1783:994–1002.
[32] Schwartz MW, Fig.lewicz DF, Kahn SE, Baskin DG, Greenwood MRC, Porte D (1990). Insulin binding to brain capillaries is reduced in genetically obese, hyperinsulinemic Zucker rats. Peptides, 11:467–472.
[33] Rodríguez JJ, Gardenal E, Zallo F, Arrue A, Cabot J, Busquets X (2024). Astrocyte S100β expression and selective differentiation to GFAP and GS in the entorhinal cortex during ageing in the 3xTg-Alzheimer's disease mouse model. Acta Histochemica, 126:152131.
[34] Pinto-Benito D, Paradela-Leal C, Ganchala D, de Castro-Molina P, Arevalo M (2022). IGF-1 regulates astrocytic phagocytosis and inflammation through the p110α isoform of PI3K in a sex-specific manner. Glia, 70:1153–1169.
[35] Geffken SJ, Moon S, Smith CO, Tang S, Lee HH, Lewis K, et al. (2022). Insulin and IGF-1 elicit robust transcriptional regulation to modulate autophagy in astrocytes. Mol Metab, 66:101647.
[36] Pedersen WA, Culmsee C, Ziegler D, Herman JP, Mattson MP (1999). Aberrant Stress Response Associated with Severe Hypoglycemia in a Transgenic Mouse Model of Alzheimer's Disease. JMN, 13:159–166.
[37] Pedrós I, Petrov D, Allgaier M, Sureda F, Barroso E, Beas-Zarate C, et al. (2014). Early alterations in energy metabolism in the hippocampus of APPswe/PS1dE9 mouse model of Alzheimer's disease. Biochim Biophys Acta, 1842:1556–1566.
[38] Vandal M, White PJ, Chevrier G, Tremblay C, St-Amour I, Planel E, et al. (2015). Age-dependent impairment of glucose tolerance in the 3xTg-AD mouse model of Alzheimer's disease. FASEB J, 29:4273–4284.
[39] Wijesekara N, Gonçalves RA, De Felice FG, Fraser PE (2018). Impaired peripheral glucose homeostasis and Alzheimer's disease. Neuropharmacology, 136:172–181.
[40] Liu X, Wang W, Chen H-L, Zhang H-Y, Zhang N-X (2019). Interplay between Alzheimer's disease and global glucose metabolism revealed by the metabolic profile alterations of pancreatic tissue and serum in APP/PS1 transgenic mice. Acta Pharmacol Sin, 40:1259–1268.
[41] Reagan LP, Cowan HB, Woodruff JL, Piroli GG, Erichsen JM, Evans AN, et al. (2021). Hippocampal-specific insulin resistance elicits behavioral despair and hippocampal dendritic atrophy. Neurobiol Stress, 15:100354.

[42] Westwell-Roper CY, Ehses JA, Verchere CB (2014). Resident macrophages mediate islet amyloid polypeptide-induced islet IL-1β production and β-cell dysfunction. Diabetes, 63:1698–1711.

[43] Kellar D, Craft S (2020). Brain insulin resistance in Alzheimer's disease and related disorders: mechanisms and therapeutic approaches. Lancet Neurol, 19:758–766.

[44] Grillo CA, Piroli GG, Lawrence RC, Wrighten SA, Green AJ, Wilson SP, et al. (2015). Hippocampal Insulin Resistance Impairs Spatial Learning and Synaptic Plasticity. Diabetes, 64:3927–3936.

[45] Spilman P, Podlutskaya N, Hart MJ, Debnath J, Gorostiza O, Bredesen D, et al. (2010). Inhibition of mTOR by Rapamycin Abolishes Cognitive Deficits and Reduces Amyloid-β Levels in a Mouse Model of Alzheimer's Disease. PLoS ONE, 5:e9979.

[46] Moro LD, Pirovano E, Rota E (2024). Mind the Metabolic Gap: Bridging Migraine and Alzheimer's disease through Brain Insulin Resistance. Aging and disease, 0.

[47] Kommaddi RP, Verma A, Muniz-Terrera G, Tiwari V, Chithanathan K, Diwakar L, et al. (2023). Sex difference in evolution of cognitive decline: studies on mouse model and the Dominantly Inherited Alzheimer Network cohort. Transl Psychiatry, 13:123.

[48] Soudy M, Bars SL, Glaab E (2025). Sex-dependent molecular landscape of Alzheimer's disease revealed by large-scale single-cell transcriptomics. Alzheimer's & Dementia, 21:e14476.

[49] Gonzalez C, Diaz F, Alonso A (2008). Neuroprotective Effects of Estrogens: Cross-Talk Between Estrogen and Intracellular Insulin Signalling. IDDT, 8:65–67.

[50] Saravia F, Beauquis J, Pietranera L, De Nicola AF (2007). Neuroprotective effects of estradiol in hippocampal neurons and glia of middle age mice. Psychoneuroendocrinology, 32:480–492.

[51] Cao L, Wang Z, Wan W (2018). Suppressor of Cytokine Signaling 3: Emerging Role Linking Central Insulin Resistance and Alzheimer's Disease. Front Neurosci, 12:417.

[52] Olloquequi J, Cano A, Sanchez-López E, Carrasco M, Verdaguer E, Fortuna A, et al. (2022). Protein tyrosine phosphatase 1B (PTP1B) as a potential therapeutic target for neurological disorders. Biomedicine & Pharmacotherapy, 155:113709.

[53] Song GJ, Jung M, Kim J-H, Park H, Rahman MH, Zhang S, et al. (2016). A novel role for protein tyrosine phosphatase 1B as a positive regulator of neuroinflammation. J Neuroinflammation, 13:86.

[54] Bélanger M, Magistretti PJ (2009). The role of astroglia in neuroprotection. Dialogues Clin Neurosci, 11:281–295.

[55] Meeker KD, Meabon JS, Cook DG (2015). Partial Loss of the Glutamate Transporter GLT-1 Alters Brain Akt and Insulin Signaling in a Mouse Model of Alzheimer's Disease. JAD, 45:509–520.

[56] Xie L, Helmerhorst E, Taddei K, Plewright B, Van Bronswijk W, Martins R (2002). Alzheimer's beta-amyloid peptides compete for insulin binding to the insulin receptor. J Neurosci, 22:RC221.

[57] Raimundo AF, Ferreira S, Martins IC, Menezes R (2020). Islet Amyloid Polypeptide: A Partner in Crime With Aβ in the Pathology of Alzheimer's Disease. Front Mol Neurosci, 13:35.

[58] De Felice FG, Vieira MNN, Bomfim TR, Decker H, Velasco PT, Lambert MP, et al. (2009). Protection of synapses against Alzheimer's-linked toxins: Insulin signaling prevents the pathogenic binding of Aβ oligomers. Proc Natl Acad Sci USA, 106:1971–1976.

[59] Schmidt AM, Stern DM (2000). Hyperinsulinemia and Vascular Dysfunction: The Role of Nuclear Factor-κB, Yet Again. Circulation Research, 87:722–724.

[60] Jong Huat T, Camats-Perna J, Newcombe EA, Onraet T, Campbell D, Sucic JT, et al. (2024). The impact of astrocytic NF-κB on healthy and Alzheimer's disease brains. Sci Rep, 14:14305.

[61] Pamies D, Sartori C, Schvartz D, González-Ruiz V, Pellerin L, Nunes C, et al. (2021). Neuroinflammatory Response to TNFα and IL1β Cytokines Is Accompanied by an Increase in Glycolysis in Human Astrocytes In Vitro. Int J Mol Sci, 22:4065.

[62] Salvadó G, Milà-Alomà M, Shekari M, Ashton NJ, Operto G, Falcon C, et al. (2022). Reactive astrogliosis is associated with higher cerebral glucose consumption in the early Alzheimer's continuum. Eur J Nucl Med Mol Imaging, 49:4567–4579.

[63] Andersen JV, Skotte NH, Christensen SK, Polli FS, Shabani M, Markussen KH, et al. (2021). Hippocampal disruptions of synaptic and astrocyte metabolism are primary events of early amyloid pathology in the 5xFAD mouse model of Alzheimer's disease. Cell Death Dis, 12:954.

[64] Elsworthy RJ, Finelli MJ, Aqattan S, Dunleavy C, King M, Ludlam A, et al. (2025). Altered metabolic function induced by Aβ-oligomers and PSEN1 mutations in iPSC -derived astrocytes. Journal of Neurochemistry, 169:e16267.

[65] Bero AW, Yan P, Roh JH, Cirrito JR, Stewart FR, Raichle ME, et al. (2011). Neuronal activity regulates the regional vulnerability to amyloid-β deposition. Nat Neurosci, 14:750–756.

[66] Carter SF, Chiotis K, Nordberg A, Rodriguez-Vieitez E (2019). Longitudinal association between astrocyte function and glucose metabolism in autosomal dominant Alzheimer's disease. Eur J Nucl Med Mol Imaging, 46:348–356.

[67] Fontana IC, Scarpa M, Malarte M-L, Rocha FM, Ausellé-Bosch S, Bluma M, et al. (2023). Astrocyte Signature in Alzheimer's Disease Continuum through a Multi-PET Tracer Imaging Perspective. Cells, 12:1469.

[68] Rodriguez-Vieitez E, Saint-Aubert L, Carter SF, Almkvist O, Farid K, Schöll M, et al. (2016). Diverging longitudinal changes in astrocytosis and amyloid PET in autosomal dominant Alzheimer's disease. Brain, 139:922–936.

[69] Logan S, Pharaoh GA, Marlin MC, Masser DR, Matsuzaki S, Wronowski B, et al. (2018). Insulin-like growth factor receptor signaling regulates working memory, mitochondrial metabolism, and amyloid-β uptake in astrocytes. Mol Metab, 9:141–155.

[70] García-Cáceres C, Quarta C, Varela L, Gao Y, Gruber T, Legutko B, et al. (2016). Astrocytic Insulin Signaling Couples Brain Glucose Uptake with Nutrient Availability. Cell, 166:867–880.

[71] Hernandez-Garzón E, Fernandez AM, Perez-Alvarez A, Genis L, Bascuñana P, Fernandez de la Rosa R, et al. (2016). The insulin-like growth factor I receptor regulates glucose transport by astrocytes. Glia, 64:1962–1971.

[72] Muhič M, Vardjan N, Chowdhury HH, Zorec R, Kreft M (2015). Insulin and Insulin-like Growth Factor 1 (IGF-1) Modulate Cytoplasmic Glucose and Glycogen Levels but Not Glucose Transport across the Membrane in Astrocytes. J Biol Chem, 290:11167–11176.

[73] Fernandez AM, Hernandez-Garzón E, Perez-Domper P, Perez-Alvarez A, Mederos S, Matsui T, et al. (2017). Insulin Regulates Astrocytic Glucose Handling Through Cooperation With IGF-I. Diabetes, 66:64–74.

[74] Leclerc M, Bourassa P, Tremblay C, Caron V, Sugère C, Emond V, et al. (2023). Cerebrovascular insulin receptors are defective in Alzheimer's disease. Brain, 146:75–90.

[75] Morant-Ferrando B, Jimenez-Blasco D, Alonso-Batan P, Agulla J, Lapresa R, Garcia-Rodriguez D, et al. (2023). Fatty acid oxidation organizes mitochondrial supercomplexes to sustain astrocytic ROS and cognition. Nat Metab, 5:1290–1302.

[76] Zyśk M, Beretta C, Naia L, Dakhel A, Påvénius L, Brismar H, et al. (2023). Amyloid-β accumulation in human astrocytes induces mitochondrial disruption and changed energy metabolism. J Neuroinflammation, 20:43.

[77] Westi EW, Jakobsen E, Voss CM, Bak LK, Pinborg LH, Aldana BI, et al. (2022). Divergent Cellular Energetics, Glutamate Metabolism, and Mitochondrial Function Between Human and Mouse Cerebral Cortex. Mol Neurobiol, 59:7495–7512.

[78] Mächler P, Wyss MT, Elsayed M, Stobart J, Gutierrez R, von Faber-Castell A, et al. (2016). In Vivo Evidence for a Lactate Gradient from Astrocytes to Neurons. Cell Metab, 23:94–102.

[79] Smolič T, Tavčar P, Horvat A, Černe U, Halužan Vasle A, Tratnjek L, et al. (2021). Astrocytes in stress accumulate lipid droplets. Glia, 69:1540–1562.

[80] Farmer BC, Walsh AE, Kluemper JC, Johnson LA (2020). Lipid Droplets in Neurodegenerative Disorders. Front Neurosci, 14:742.

[81] Chen Y, Zhao Y, Dai C, Liang Z, Run X, Iqbal K, et al. (2014). Intranasal insulin restores insulin signaling, increases synaptic proteins, and reduces Aβ level and microglia activation in the brains of 3xTg-AD mice. Experimental Neurology, 261:610–619.

[82] Mao Y, Guo Z, Zheng T, Jiang Y, Yan Y, Yin X, et al. (2016). Intranasal insulin alleviates cognitive deficits and amyloid pathology in young adult APP swe/ PS 1dE9 mice. Aging Cell, 15:893–902.

[83] Stine WB, Jungbauer L, Yu C, LaDu MJ (2010). Preparing Synthetic Aβ in Different Aggregation States. In: Roberson ED, editor Alzheimer's Disease and Frontotemporal Dementia. Totowa, NJ: Humana Press, 13–32.

[84] Hu X, Crick SL, Bu G, Frieden C, Pappu RV, Lee J-M (2009). Amyloid seeds formed by cellular uptake, concentration, and aggregation of the amyloid-beta peptide. Proc Natl Acad Sci USA, 106:20324–20329.

[85] Berry BJ, Smith AST, Long CJ, Martin CC, Hickman JJ (2018). Physiological Aβ Concentrations Produce a More Biomimetic Representation of the Alzheimer's Disease Phenotype in iPSC Derived Human Neurons. ACS Chem Neurosci, 9:1693–1701.